Distribution and magnitude of stress due to lateral variation of gravitational potential energy between Indian lowland and Tibetan plateau

Stefan M. Schmalholz [1], Thibault Duretz,[1,2] György Hetényi [1] and Sergei Medvedev[3]

[1]*Institute of Earth Sciences, University of Lausanne,* 1015 *Lausanne, Switzerland. E-mail:* stefan.schmalholz@unil.ch
[2]*Univ Rennes, CNRS, Géosciences Rennes—UMR* 6118, *F-*35000 *Rennes, France*
[3]*Centre for Earth Evolution and Dynamics, University of Oslo, N-*0315 *Oslo, Norway*

SUMMARY

Magnitudes of differential stress in the lithosphere, especially in the crust, are still disputed. Earthquake-based stress drop estimates indicate median values <10 MPa whereas the lateral variation of gravitational potential energy per unit area (*GPE*) across significant relief indicates stress magnitudes of *ca.* 100 MPa in average across a 100 km thick lithosphere between the Indian lowland and the Tibetan plateau. These standard *GPE*-based stress estimates correspond to membrane stresses because they are associated with a deformation that is uniform with depth. We show here with new analytical results that lateral variations in *GPE* can also cause bending moments and related bending stresses of several hundreds of MPa. Furthermore, we perform 2-D thermomechanical numerical simulations (1) to evaluate estimates for membrane and bending stresses based on *GPE* variations, (2) to quantify minimum crustal stress magnitudes that are required to maintain the topographic relief between Indian lowland and Tibetan plateau for *ca.* 10 Ma and (3) to quantify the corresponding relative contribution of crustal strength to the total lithospheric strength. The numerical model includes viscoelastoplastic deformation, gravity and heat transfer. The model configuration is based on density fields from the CRUST1.0 data set and from a geophysically and petrologically constrained density model based on *in situ* field campaigns. The numerical results indicate that values of differential stress in the upper crust must be >*ca.* 180 MPa, corresponding to a friction angle of *ca.* 10° to maintain the topographic relief between lowland and plateau for >10 Ma. The relative contribution of crustal strength to total lithospheric strength varies considerably laterally. In the region between lowland and plateau and inside the plateau the depth-integrated crustal strength is approximately equal to the depth-integrated strength of the mantle lithosphere. Simple analytical formulae predicting the lateral variation of depth-integrated stresses agree with numerically calculated stress fields, which show both the accuracy of the numerical results and the applicability of simple, rheology-independent, analytical predictions to highly variable, rheology-dependent stress fields. Our results indicate that (1) crustal strength can be locally equal to mantle lithosphere strength and that (2) crustal stresses must be at least one order of magnitude larger than median stress drops in order to support the plateau relief over a duration of *ca.* 10 Ma.

Key words: Numerical modelling; Continental tectonics: compressional; Dynamics: gravity and tectonics; Mechanics, theory, and modelling; Rheology: crust and lithosphere.

1 INTRODUCTION

The magnitude and vertical distribution of stress in the continental lithosphere and the associated vertical distribution of strength control the deformation behaviour of the lithosphere. For example, a mechanically stronger lithosphere exhibits a larger flexural wavelength than a weaker one (e.g. Burov & Diament 1995). Also, during long-term lithospheric deformation significant deviatoric stresses can potentially generate sufficient dissipative work so that thermal softening can trigger lithospheric-scale strain localisation (e.g.
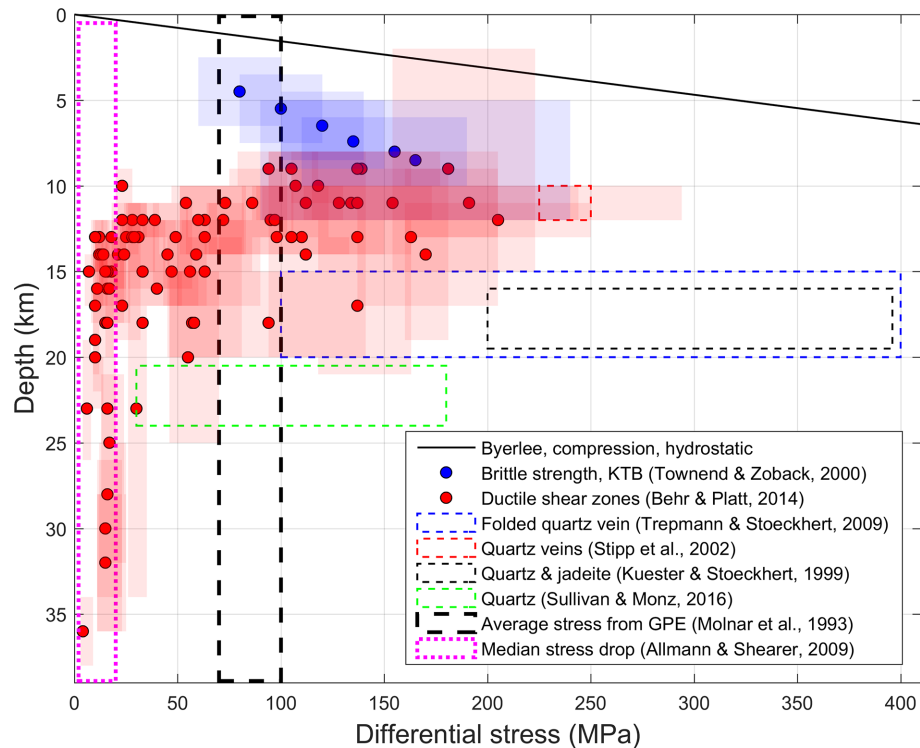
Figure 1. Differential stress estimates for the crust. The solid black line shows differential stress based on Byerlee's law for compression and hydrostatic fluid pressure (see e.g. Kohlstedt *et al.* 1995). Blue circles indicate stress estimates from the KTB borehole after Townend & Zoback (2000) and transparent blue rectangles indicate the reported uncertainty range. The KTB borehole data are for a regional strike-slip regime (Brudy *et al.* 1997). Red circles indicate piezometer estimates from ductile shear zones after Behr & Platt (2014) and transparent red rectangles indicate the reported uncertainty range. Blue dashed rectangle indicates the range of stress estimated from microstructure in a folded quartz vein after Trepmann & Stöckhert (2009). Red dashed rectangle indicates the range of stress estimated from microstructure in quartz veins after Stipp *et al.* (2002). Black dashed rectangle indicates the range of stress estimated from microstructure in quartz, jadeite, omphacite and calcite after Kuester & Stöckhert (1999). Green dashed rectangle indicates the range of stress estimated from microstructure in quartz after Sullivan & Monz (2016). Thick black dashed vertical rectangle indicates the range of depth-averaged (over 100 km thickness) stress estimated from lateral *GPE* variations after Molnar *et al.* (1993). Thick dotted magenta line indicates the median of earthquake-based stress drop estimates range after Allmann & Shearer (2009).

Schmalholz *et al.* 2009; Jaquet *et al.* 2016) and subduction initiation (e.g. Thielmann & Kaus 2012). Furthermore, if differential stresses exist in the lithosphere then the stress state is neither hydrostatic nor lithostatic. Rock deformation experiments show that such non-hydrostatic stresses can affect mineral transformations, such as the quartz-coesite transition (Hirth & Tullis 1994; Richter *et al.* 2016), and differential stresses could, hence, affect mineral phase transformations in the lithosphere (e.g. Moulas *et al.* 2014; Moulas *et al.* 2018; Tajčmanová *et al.* 2015). Conversely, metamorphic phase changes accompanied by volume change affect the stress and deformation field (e.g. Hetényi *et al.* 2011; Hetényi 2014). Consequently, the commonly performed conversion of metamorphic pressure to burial depth, assuming a lithostatic stress state, could be significantly inaccurate (e.g. Petrini & Podladchikov 2000; Schmalholz & Podladchikov 2013; Moulas *et al.* 2014; Moulas *et al.* 2018).

The above examples show that stress magnitudes can potentially have significant impact on lithospheric deformation and associated metamorphic processes. However, these stress magnitudes are still controversially debated, particularly stress magnitudes in the crust. For example, estimates of differential stress in the upper crust, which are based on *in situ* stress measurements in deep wells and a borehole of the German Continental Deep Drilling Program (KTB), indicate differential stress between 170 and 210 MPa at a depth of approximately 8 km (e.g. Brudy *et al.* 1997; Townend & Zoback 2000; Fig. 1). Also, differential stress in natural shear zones estimated

from grain size piezometers (e.g. Twiss 1977) can reach a few hundred MPa in crustal depths of 5–25 km (see Fig. 1 and references in caption). Such differential stress estimates from piezometers agree with flow laws for dislocation creep for quartzite and limestone (e.g. Behr & Platt 2014; Jaquet & Schmalholz 2018).

In contrast to the above stress estimates, earthquake-based stress drop estimates range typically between 0.3 and 50 MPa with a median stress drop of *ca.* 4 MPa for depths less than 60 km (e.g. Allmann & Shearer 2006; Fig. 1). The histogram of the logarithmic stress drop estimates of Allmann & Shearer (2006; their Fig. 6) indicates a standard deviation of stress drops from 1 to 10 MPa (Fig. 1). The stress drop usually refers to a drop in shear stress, which is approximately half the differential stress. It is, however, not clear whether stress drop magnitudes are close to total stress drop or whether the stress drop only represents a small fraction of the crustal stress (e.g. McGarr & Gay 1978; Kanamori 1980; Hardebeck & Okada 2018). Stress drop estimates require assumptions on fault geometry, which is usually not well known, and errors concerning fault plane geometry can cause large errors in the corresponding stress drop estimate (e.g. Madariaga 1977). Furthermore, the static stress drop estimated by seismologists provides a lower bound to the actual dynamic stress drop on the fault occurring during dynamic fracturing (e.g. Madariaga 1977). The analysis of pseudotachylyte fault veins, commonly considered to represent 'palaeoearthquakes', indicates that stress drop can be greater than
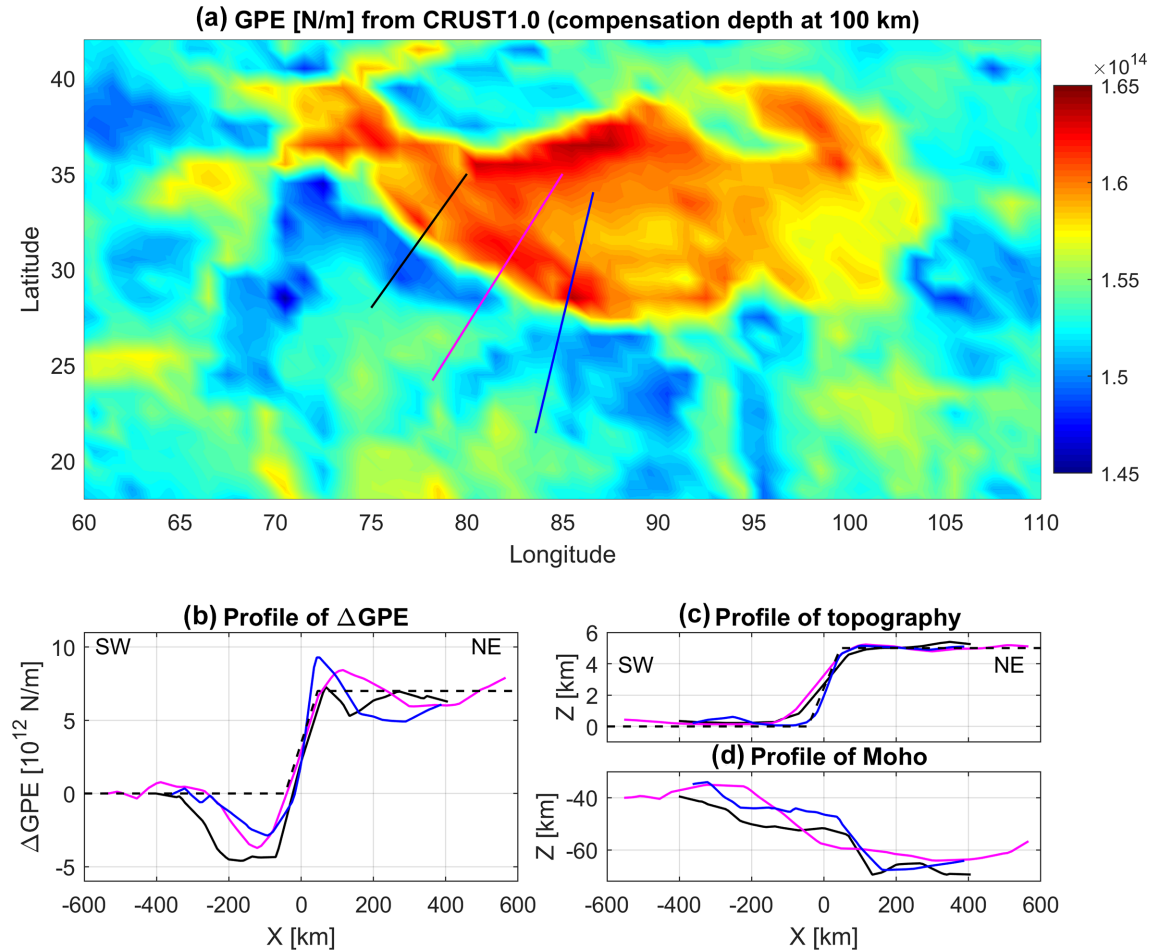
(a) GPE [N/m] from CRUST1.0 (compensation depth at 100 km)

Figure 2. (a) Colour plot of GPE (N m^{-1}) for the region around the Tibetan plateau (region mainly in red). Values of GPE have been calculated directly from the CRUST1.0 data set (http://igppweb.ucsd.edu/~gabi/rem.html), namely from the given densities and depths of the crustal units. Values of GPE were calculated using eqs (6) and (13) assuming a compensation depth, Sb, at 100 km and no corrections have been applied to the CRUST1.0 data. Three profiles (solid black, magenta and blue lines) have been calculated for the corresponding $\triangle GPE$ (b), topography (c) and crust–mantle boundary depth (Moho, d). (b) Three profiles of $\triangle GPE$ (see panel a for location). The value of GPE from the leftmost position ($X = -600$ km) has been subtracted from all other values of GPE to generate values of $\triangle GPE$. The dashed black line corresponds to the initial profile of $\triangle GPE$ corresponding to the performed numerical simulation initially in isostasy. (c) Three profiles (see panel a for location) of topography taken directly from the CRUST1.0 data set without corrections. (d) Three profiles (see panel a for location) of Moho depth taken directly from the CRUST1.0 data set without corrections.

220 MPa and as high as 580 MPa (Andersen *et al.* 2008), which also suggests that earthquake-based stress drop estimates provide lower bounds to the actual stress.

Another method to estimate lithospheric stress magnitudes is based on vertical integrals of the force balance equations for the lithosphere. Models based on vertical integrals of the force balance equations are commonly referred to as thin-sheet models (e.g. England & McKenzie 1982; Medvedev & Podladchikov 1999a). Based on such thin-sheet models, the vertical integral of the differential stress in the lithosphere can be estimated from the lateral variation of crustal thickness and topography (e.g. Jeffreys 1959; Arthyushkov 1973) or, more generally, from lateral variations of the gravitational potential energy per unit area (GPE; e.g. Molnar & Lyon-Caen 1988; Molnar *et al.* 1993; Schmalholz *et al.* 2014). These integrated stress estimates result from force balance calculations only and are robust because they are independent on constitutive equations (e.g. flow laws), that is, irrespective of the lithosphere deformation being elastic, plastic or viscous. Consequently, lateral GPE variations can be used only to calculate the vertical integral

of the stress, which can be related to the horizontal driving force per unit length (F_x; e.g. Molnar & Lyon-Caen 1988), but not maximum stress magnitudes in the lithosphere. Also, standard thin-sheet models assume that the deformation is uniform with depth so that horizontal stresses along a vertical profile are either all compressive or extensive. Stresses associated with a depth-uniform deformation are commonly referred to as membrane, or in-plane, stresses. When integrated vertically, all membrane stresses contribute to F_x. Stresses associated with bending (or flexure) of the lithosphere are neglected in standard thin-sheet models. Bending stresses typically change their sign across a bending layer, for example, due to extension in the outer hinge region and compression in the inner region. Since bending stresses change their sign along a vertical profile they usually do not contribute significantly during vertical stress integration to F_x and are, hence, not estimated from standard lateral GPE variations. We show here with new analytical relations that lateral GPE variations are associated with bending moments due to lateral mass variations and that these mass moments cause significant bending stresses.
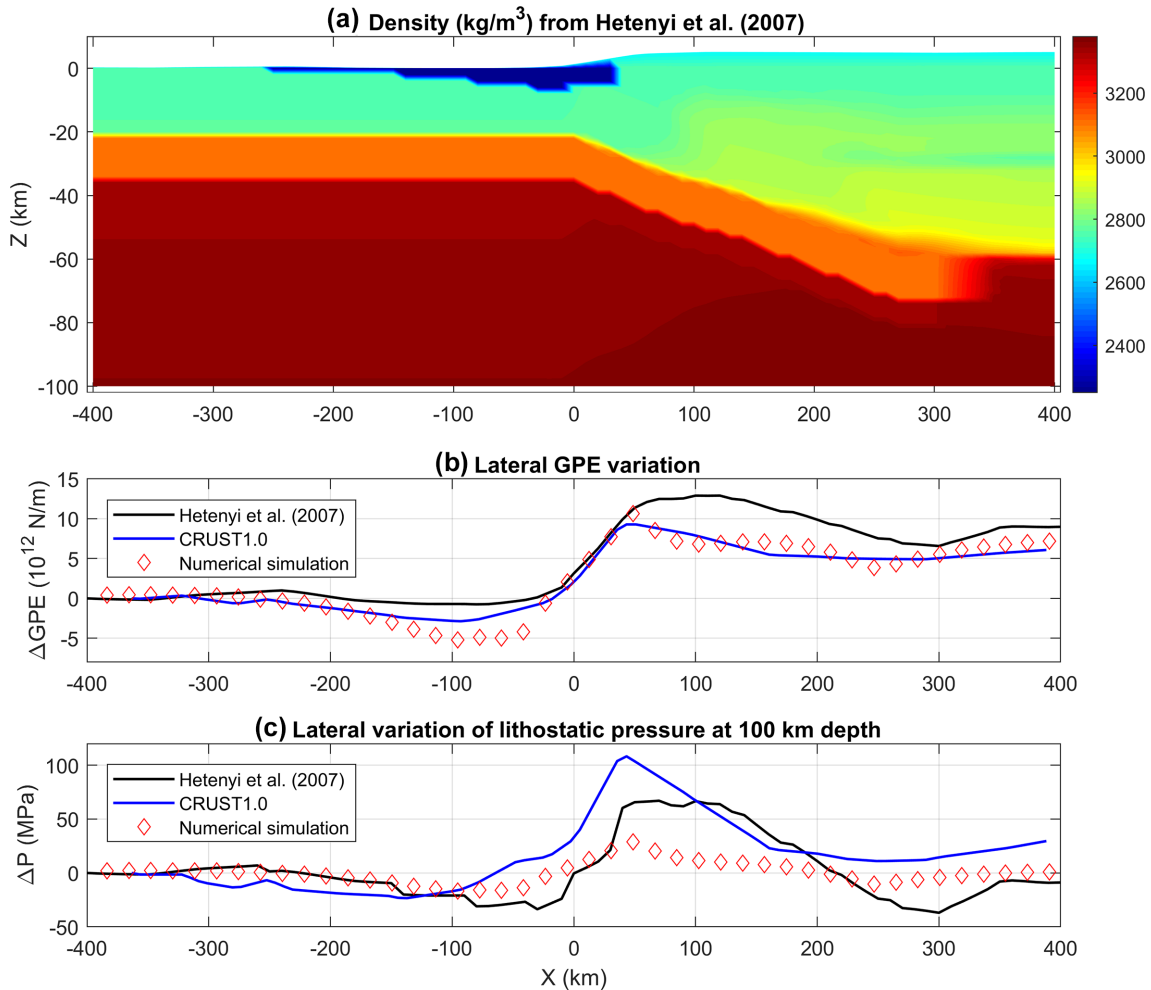
Figure 3. (a) Colour plot of density distribution from Hetényi *et al.* (2007). The location of the corresponding profile is indicated by the blue line in Fig. 2(a). (b) Lateral variation of ΔGPE for the density profile in panel (a) (black line) and for the corresponding density profile along the same section of the CRUST1.0 data (blue line). The red diamonds show values of ΔGPE corresponding to the numerical simulation 1 (crustal friction angle of 10° and Moho transition width of 300 km; Figs 6a–c) at 8 Ma. (c) Lateral variation of lithostatic pressure at 100 km depth corresponding to the density profile in panel (a) (black line) and for the corresponding density profile along the same section of the CRUST1.0 data (blue line). The red diamonds show the lateral variation of lithostatic pressure at the model depth (300 km) corresponding to the numerical simulation 1 (crustal friction angle of 10° and Moho transition width of 300 km; Figs 6a–c) at 8 Ma. The lateral variation of lithostatic pressure corresponds to the tectonic pressure, that is, rock pressure minus lithostatic pressure.

Lateral *GPE* variations between the Tibetan plateau and the Indian lowland, referring to the hinterland and foreland of the Himalaya, respectively, provide estimates of *ca.* 7×10^{12} N m^{-1} for F_x (e.g. Molnar & Lyon-Caen 1988; Fig. 2) and between Tibet and Central Asia estimates of $7 - 10 \times 10^{12}$ N m^{-1} (e.g. Molnar *et al.* 1993; England & Molnar 2015). If one assumes that a representative value for the thickness of the lithosphere is 100 km then the above estimates of F_x provide depth-average differential stresses between 70 and 100 MPa in the lithosphere. However, due to considerable rheological variations within the lithosphere, local stresses can be significantly smaller or larger than these depth-averaged estimates (see examples for the flexure of the Indian plate, e.g. Cattin *et al.* 2001; Hetényi *et al.* 2006). Furthermore, the relative contribution, or fraction, of stresses in the crust and mantle lithosphere to the total integrated stress across the lithosphere is usually unknown. England & Molnar (2015) suggest that values of F_x acting on the lithosphere of the Tien Shan are $7–10 \times 10^{12}$ N m^{-1} and they argue that a significant fraction, up to 90 per cent, of F_x is provided by the ductile mantle lithosphere. If the continental crust would indeed

only provide a small fraction of the lithospheric resistance to F_x, then the question arises: how can such a weak crust maintain for *ca.* 10 Ma the significant lateral variations in surface topography and *GPE* between the Tibetan plateau and Indian lowland (Figs 2 and 3)? The main aim of our study is to quantify with 2-D thermomechanical numerical simulations the magnitudes of differential stress in the crust that are required to maintain the relief of the Tibetan plateau for a duration of *ca.* 10 Ma. Furthermore, bending of the lithosphere generates likely the largest stress magnitudes on Earth compared with other geophysical processes such as mantle convection (e.g. Karato 2008; his table 19.2). Medvedev (2016) suggested that lateral variations of *GPE* may result in lithospheric bending stresses and that these stresses may dominate the orientation of stresses even in the absence of compressive deformation such as lithospheric folding. Therefore, we also investigate the influence of bending on the stress state of the India–Himalaya–Tibet system because we are interested in estimates for local, maximum stress magnitudes.
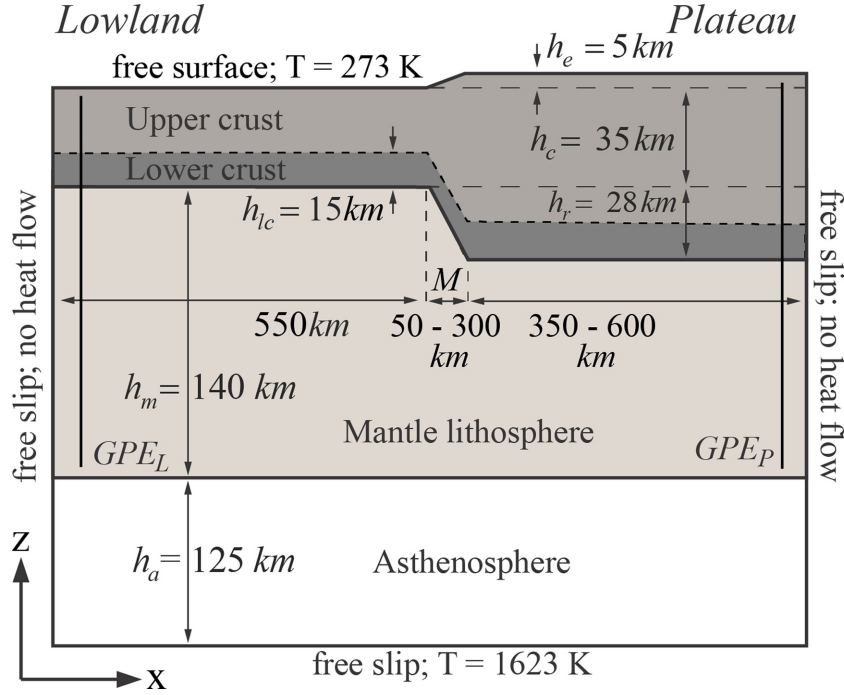
Figure 4. Model configuration for both the 2-D numerical simulations and the analytical thin-sheet results. The h_e is the initial topography of the plateau with respect to the lowland, h_c is the total crustal thickness of the lowland, h_r is the thickness of the crustal root (including the lower crust) below the plateau, h_{lc} is the thickness of the lower crust, h_m is the thickness of the mantle lithosphere below the lowland and h_a is the thickness of the asthenosphere layer. M is the width of the transition zone of the crust–mantle boundary (Moho) in which the Moho deepens from 35 to 68 km depth below topography. M can vary from 50 to 300 km in the different simulations. The transition zone of the topographic variation has always a width of 100 km. For the analytical results, the values of GPE_L and GPE_P have been calculated for a constant density in the upper and lower crust of 2800 kg m^{-3} and for constant density of the mantle lithosphere of 3300 kg m^{-3}.

We perform 2-D numerical simulations considering viscoelasto-plastic deformation, heat transfer, gravity, and temperature dependent flow laws to calculate the distribution of stresses in a continental lithosphere caused by interaction of a plateau and neighbouring lowland in the absence of any additional tectonic influence. The initial lithosphere geometry is close to the standard geometry of thin-sheet models, which were used to calculate the lateral *GPE* variation between India and Tibet (e.g. Molnar & Lyon-Caen 1988; Molnar *et al.* 1993; Schmalholz *et al.* 2014), and to construct a gravimetrically and petrologically constrained density model of the Indian plate beneath the Tibetan plateau (Hetényi *et al.* 2007). We also compare the lateral variation of depth-integrated numerical stresses with predictions of analytical thin-sheet models to show the accuracy and robustness of the numerical results.

2 STRESS RELATIONS, GRAVITATIONAL POTENTIAL ENERGY AND BENDING

2.1 Lithospheric stress relations

For incompressible deformation in 2-D, the components of the total stress tensor are

$$\sigma_{xx} = -P + \tau_{xx}$$
$$\sigma_{zz} = -P + \tau_{zz} \quad (1)$$
$$\sigma_{xz} = \tau_{xz}$$

where pressure, or negative mean stress, $P = -(\sigma_{xx} + \sigma_{zz})/2$, $\tau_{xx} = -\tau_{zz}$ are the normal deviatoric stress tensor components, $\sigma_{xz} = \tau_{xz}$ represents the shear stress and x and z are the horizontal

and vertical coordinates, respectively. The maximum, σ_1, and minimum, σ_3, principal stresses are (e.g. Turcotte & Schubert 2014)

$$\sigma_1 = \frac{\sigma_{xx} + \sigma_{zz}}{2} + \left[\frac{(\sigma_{xx} - \sigma_{zz})^2}{4} + \tau_{xz}^2 \right]^{\frac{1}{2}}$$
$$= -P + \left[\tau_{xx}^2 + \tau_{xz}^2 \right]^{\frac{1}{2}} = -P + \tau_{\text{II}} \quad (2)$$

$$\sigma_3 = \frac{\sigma_{xx} + \sigma_{zz}}{2} - \left[\frac{(\sigma_{xx} - \sigma_{zz})^2}{4} + \tau_{xz}^2 \right]^{\frac{1}{2}}$$
$$= -P - \left[\tau_{xx}^2 + \tau_{xz}^2 \right]^{\frac{1}{2}} = -P - \tau_{\text{II}}, \quad (3)$$

where τ_{II} is the square root of the second invariant of the deviatoric stress tensor. The differential stress is

$$\Delta\sigma = \sigma_1 - \sigma_3 = 2\tau_{\text{II}}. \quad (4)$$

Following Molnar & Lyon-Caen (1988) and Schmalholz *et al.* (2014) we separate the total normal horizontal stress into two components:

$$\sigma_{xx} = \sigma_{xx}^{\text{s}} + \sigma_{xx}^{\text{d}}, \quad (5)$$

where the static stress, σ_{xx}^{s}, is identical to the negative of the lithostatic pressure, P_{L}, or hydrostatic stress, which is the vertical integral of the product of density, ρ, times gravitational acceleration, g:

$$\sigma_{xx}^{\text{s}}(x, z) = -P_{\text{L}}(x, z) = -\int_z^{St(x)} \rho(x, z') \, g \mathrm{d}z' \quad (6)$$

with $St(x)$ being the topography, which can vary laterally. The dynamic component of the total stress in eq. (5), σ_{xx}^{d}, thus represents
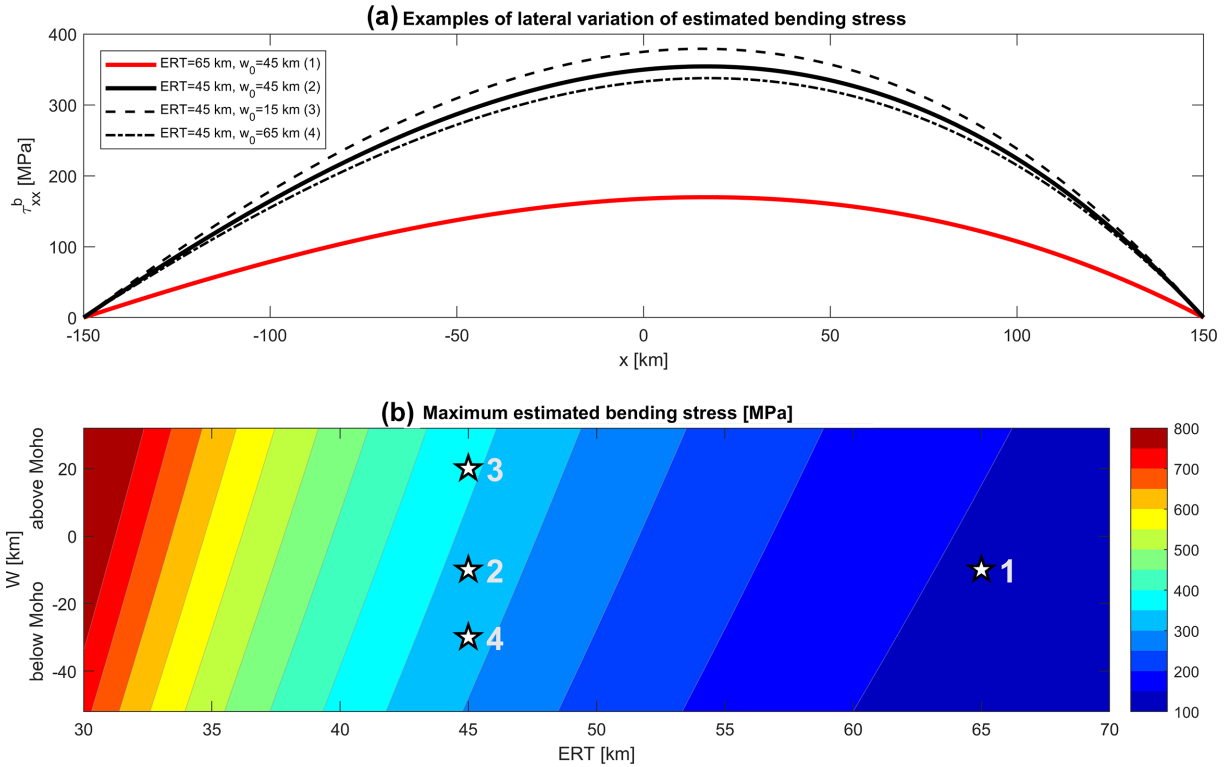
Figure 5. (a) Lateral variation of estimated bending stresses (eq. 28) for specific values of effective rheological thickness, ERT, and for specific position of the neutral reference line, w (eqs 20 and 21), which is set parallel to the Moho. w_0 is the depth of w in the lowland. (b) Each bending stress profile has a maximum stress. These maximum bending stresses are contoured in the space ERT versus W. W is the distance of the neutral reference line, w, from the Moho. The four profiles displayed in panel (a) are indicated by the corresponding numbered stars. The maximum bending stress depends to first order on the ERT.
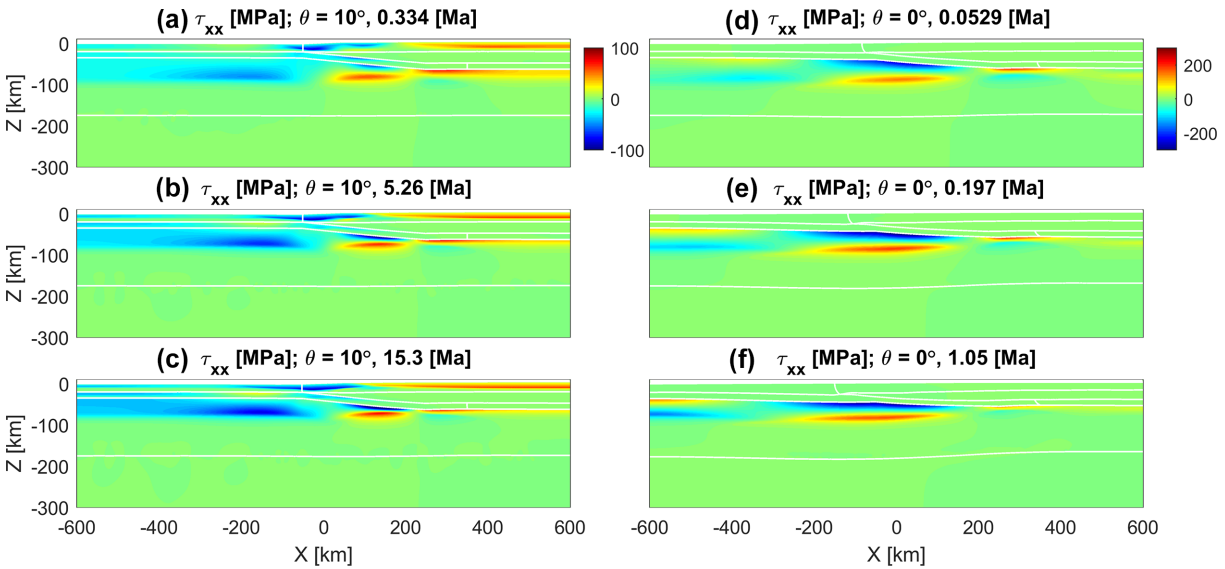

Figure 6. Colour plot of horizontal deviatoric stress, τ_{xx} (MPa), for three different times for simulation 1 with a friction angle in the crust of 10° (a–c) and simulation 2 with 0° (d–f), both for $M = 300$ km. Negative values indicate compression, positive ones extension and the legends at the top right of the two columns (a–c and d–f) apply to the entire column. The entire model domain is shown. Times in million years (Ma) indicate the duration of the simulations. In each panel, the lowermost horizontal white line indicates the lithosphere/asthenosphere boundary, the middle white line indicates the base of the lower crust (Moho) and the uppermost white line indicates the upper/lower crustal boundary. The two short vertical white lines in the upper and lower crust are passive marker lines, which indicate horizontal flow in the crust.

a measure of how far the stresses in the lithosphere deviate from the lithostatic state.

The above stress relations are exact and free from assumptions. In order to simplify calculations, several approximate stress relations

are assumed in traditional thin-sheet approximations (e.g. England & McKenzie 1982, Schmalholz *et al.* 2014). The main assumption is that shear stress, τ_{xz}, can be neglected when considering the large-scale lithospheric stress state. The approximate equalities in

the following equations are based on this assumption of negligible τ_{xz}. The total normal vertical stress can then be approximated by the lithostatic pressure:

$$\sigma_{zz} \approx -P_{\mathrm{L}}. \tag{7}$$

The relation between dynamic horizontal stress and deviatoric horizontal stress is then

$$\sigma_{xx}^{\mathrm{d}} = \sigma_{xx} + P_{\mathrm{L}} \approx \tau_{xx} - P - \sigma_{zz} = \tau_{xx} - \tau_{zz} = 2\tau_{xx}. \tag{8}$$

Eq. (8) shows that $\sigma_{xx}^{\mathrm{d}} \approx 2\tau_{xx}$, which is relevant because it explains the factor two difference in stress magnitudes obtained from lateral *GPE* variations around the Tibetan plateau by Molnar & Lyon-Caen (1988), who calculated σ_{xx}^{d}, and stress magnitudes obtained by Ghosh *et al.* (2006, 2009), who calculated τ_{xx} (Schmalholz *et al.* 2014). The condition of negligible τ_{xz} results in the principal stress axes to be close to the vertical and horizontal orientations and thus eq. (4) can be approximated

$$\Delta\sigma = \sigma_1 - \sigma_3 \approx \mathrm{abs}\,(\sigma_{xx} - \sigma_{zz}) \approx \mathrm{abs}\,(\sigma_{xx}^{\mathrm{d}}). \tag{9}$$

2.2 *GPE* and thin-sheet relations

Integration of the horizontal balance of stresses from the top stress-free surface $St(x)$ down to the horizontally constant depth of compensation, Sb, at which the deviatoric stresses can be neglected, reveals the absence of the lateral variation of the depth-integrated horizontal total stress, σ_{xx} (Molnar & Lyon-Caen 1988; Schmalholz *et al.* 2014):

$$\frac{\mathrm{d}}{\mathrm{d}x}\,(\bar{\sigma}_{xx}) = 0. \tag{10}$$

Here, an overbar indicates the depth integral of the corresponding symbol, for example,

$$\bar{\sigma}_{xx}\,(x) = \int_{Sb}^{St(x)} \sigma_{xx}\,(x, z)\,\mathrm{d}z. \tag{11}$$

Eq. (10) is not based on the thin-sheet approximation presented in Section 2.1 and is thus fundamental. For example, it was shown that eq. (10) holds for a numerically calculated 2-D stress field of a shortening viscoelastoplastic lithosphere involving buckling and shear zone generation (Schmalholz & Podladchikov 2013). Eq. (10), however, is based on the condition of vanishing deviatoric stresses at the bottom boundary, Sb, which is a reasonable assumption at the lithosphere–asthenosphere transition. Consequently, Sb is often termed the depth of the lithosphere in the framework of depth-integrated stress analysis, although Sb differs from traditional geological and geophysical definitions of the lithosphere–asthenosphere boundary (e.g. Turcotte & Schubert 2014). Substitution of the separation of the normal horizontal stress into static and dynamic components, eqs (5) and (6), into eq. (10) yields (e.g. Molnar & Lyon-Caen 1988; Schmalholz *et al.* 2014)

$$\frac{\mathrm{d}}{\mathrm{d}x} F_x = \frac{\mathrm{d}}{\mathrm{d}x} GPE, \tag{12}$$

where $F_x = \bar{\sigma}_{xx}^{d}$ is commonly termed the driving horizontal force per unit length and the *GPE* is the vertical integral of P_{L}:

$$GPE\,(x) = \bar{P}_L\,(x) + \mathrm{const} = \int_{Sb}^{St(x)} P_L\,(x, z)\,\mathrm{d}z + \mathrm{const}. \tag{13}$$

Eq. (12) can be integrated with respect to x and for a simple geometry with essentially only a plateau and lowland (Fig. 4) the horizontal derivatives in eq. (12) can be replaced by horizontal

differences, indicated with the symbol Δ, between values for the plateau and the lowland, for example, $\Delta GPE = GPE_{\mathrm{P}} - GPE_{\mathrm{L}}$ (Fig. 4):

$$\Delta F_x = \Delta GPE. \tag{14}$$

Therefore, ΔGPE can be related to vertically integrated stress differences by

$$\Delta GPE = \Delta\bar{\sigma}_{xx}^{\mathrm{d}} \approx 2\Delta\bar{\tau}_{xx}. \tag{15}$$

Similar to Section 2.1, we use the approximate equality sign to indicate the thin-sheet assumption of negligible τ_{xz}. The lateral variation in *GPE* assuming local isostasy at the base of the lithosphere and uniform densities within the crust, ρ_{c}, and mantle lithosphere, ρ_{m}, is (e.g. Molnar & Lyon-Caen 1988; Schmalholz *et al.* 2014)

$$\Delta GPE = \rho_{\mathrm{c}} g h_{\mathrm{e}} \left(h_{\mathrm{c}} + \frac{\rho_{\mathrm{m}}}{\rho_{\mathrm{m}} - \rho_{\mathrm{c}}} \frac{h_{\mathrm{e}}}{2} \right), \tag{16}$$

where h_{e} and h_{c} are the height of the plateau with respect to the one of the lowland and the crustal thickness of the lowland, respectively (Fig. 4).

The above estimations operate with depth-integrated stresses whereas the magnitude of stresses is the target of our study. Strong rheological heterogeneity of the lithosphere results in strong variations of stresses with depth. Most of the integrated lithospheric stress quantities, such as F_x, are controlled by stresses in the strong levels of the lithosphere (e.g. Burov 2011). The magnitudes of the stresses within these stress-bearing levels are the focus of our study. Similar to the effective elastic thickness, which characterizes an elastic lithospheric model (e.g. Burov & Diament 1995), we introduce here the effective rheological thickness (ERT) of the lithosphere, which is independent of a particular rheological model. A formal definition of ERT is out of the scope of our study. We use a more qualitative approach here to illustrate the results of analytical studies and compare them with 2-D thermomechanical numerical results in the following sections. The scope of the analytical study, which is independent on any rheology assumption, is to obtain a comparison with the numerical results, which are calculated for specific rheological models. The difference of the characteristic deviatoric stress is by definition, and using eqs (14)–(16)

$$\Delta\tau_{xx}^* = \frac{\Delta F_x}{2ERT} = \frac{\rho_{\mathrm{c}} g h_{\mathrm{e}}}{2ERT} \left(h_{\mathrm{c}} + \frac{\rho_{\mathrm{m}}}{\rho_{\mathrm{m}} - \rho_{\mathrm{c}}} \frac{h_{\mathrm{e}}}{2} \right). \tag{17}$$

To illustrate the usage of ERT, we assume that the crust is much stronger than other regions of the lithosphere (Fig. 4) and that ERT is equal to the crustal thickness averaged between plateau and lowland, that is, $ERT = h_{\mathrm{c}} + (h_{\mathrm{e}} + h_{\mathrm{r}})/2$. We also assume that characteristic deviatoric stresses in the plateau and lowland are identical, but opposite in sign, so that $\tau_{xx}^* = \Delta\tau_{xx}^*/2$ (Schmalholz *et al.* 2014). Using the isostasy relation $h_{\mathrm{r}} = \rho_{\mathrm{c}} h_{\mathrm{e}}/(\rho_{\mathrm{m}} - \rho_{\mathrm{c}})$ eq. (17) yields

$$\tau_{xx}^* = \frac{\rho_{\mathrm{c}} g h_{\mathrm{e}}}{4}. \tag{18}$$

This result indicates that the average deviatoric stress in the crust is directly proportional to the topographic relief. For $h_{\mathrm{e}} = 5$ km and $\rho_{\mathrm{c}} = 2800$ kg m^{-3} one obtains $\tau_{xx}^* = ca.$ 35 MPa which is a value that is nearly one order of magnitude larger than the median stress drop of *ca.* 4 MPa estimated from earthquakes.

The above estimations of the characteristic membrane, or in-plane, stresses assume the homogeneous deformation with depth of the lithosphere so that the stresses do not change their sign with depth and additively contribute to the integrated stress. This depth-uniform deformation may be associated with the traditional thin-sheet approximation (England & McKenzie 1982).

2.3 Bending stresses related to lateral variations of *GPE*

Lateral variations of GPE are associated with the laterally varying distribution of mass. This lateral mass variation can also result in moments of forces, which can cause bending stresses. The numerical simulations performed in this study will show bending related stresses and we derive here fundamental relations between GPE and bending stresses to estimate the order of magnitude of these bending stresses, independent of any rheological assumptions.

Schmalholz *et al.* (2014) presented the integration of the vertical balance of stresses in a form that links the lateral variation of the tectonic pressure, P_O (the difference between P and P_L, $P_O = P - P_L$), at depth Sb with the horizontal derivative of the depth-integrated shear stress:

$$P_O(x, Sb) = \frac{\mathrm{d}}{\mathrm{d}x}(\bar{\tau}_{xz}). \tag{19}$$

In the absence of horizontal tractions along the top and bottom boundaries, the integrated shear stress $\bar{\tau}_{xz}$ can be related to the total horizontal stress, σ_{xx}, by the following equation (e.g. Schmalholz & Mancktelow 2016; their eq. A14)

$$\bar{\tau}_{xz} = \frac{\mathrm{d}}{\mathrm{d}x}\Pi(\sigma_{xx}) + \bar{\sigma}_{xx}\frac{\mathrm{d}w}{\mathrm{d}x}. \tag{20}$$

The bending moment, $\prod$, associated with any stress component, σ_{ij}, and with the vertical coordinate of a neutral reference line, $w(x)$, is

$$\prod(\sigma_{ij}) = \int_{Sb}^{St(x)} \sigma_{ij}(z-w)\,\mathrm{d}z = \overline{\sigma_{ij}(z-w)}. \tag{21}$$

Separating σ_{xx} into dynamic and static components, eq. (5), substituting eq. (20) into eq. (19), and using eq. (10) yields

$$P_O(x, Sb) = \frac{\mathrm{d}^2}{\mathrm{d}x^2}\Pi(\sigma_{xx}^d) + \bar{\sigma}_{xx}\frac{\mathrm{d}^2w}{\mathrm{d}x^2} - \frac{\mathrm{d}^2}{\mathrm{d}x^2}\Pi(P_L). \tag{22}$$

Eq. (22) indicates that the existence of tectonic pressure at the base of the model, $P_O(x, Sb)$, is related to bending moments and flexure in the model domain. To estimate the bending, or fibre, stress we decompose the dynamic stress into a membrane stress, σ_{xx}^{ts}, and a bending stress, σ_{xx}^b, that is, $\sigma_{xx}^d = \sigma_{xx}^{ts} + \sigma_{xx}^b$ (e.g. Schmalholz & Podladchikov 2000, their Fig. 1; Schmalholz & Mancktelow 2016, their eq. A19). The membrane stress, σ_{xx}^{ts}, corresponds to the depth-uniform thin-sheet deformation and is constrained by conditions $\bar{\sigma}_{xx}^d = \bar{\sigma}_{xx}^{ts}$ and $\prod(\sigma_{xx}^{ts}) = 0$. The bending stress, σ_{xx}^b, represents the deviation from σ_{xx}^{ts} due to bending and is constrained by the conjugate conditions $\bar{\sigma}_{xx}^b = 0$ and $\prod(\sigma_{xx}^d) = \prod(\sigma_{xx}^b)$. In Appendix A, we show that this separation is possible by the appropriate choice of the reference level, $w(x)$. As illustrative example we assume that $w(x)$ is a piecewise linear function of x as, for example, the lateral variation of the crust–mantle boundary in the model configuration of Fig. 4. Assuming furthermore local isostasy (i.e. $P_O(x, Sb) = 0$), eq. (22) reduces to

$$\frac{\mathrm{d}^2}{\mathrm{d}x^2}\Pi(\sigma_{xx}^b) = \frac{\mathrm{d}^2}{\mathrm{d}x^2}\Pi(P_L). \tag{23}$$

The term with $\mathrm{d}^2w/\mathrm{d}x^2$ has disappeared due to the assumption of piecewise linearity of $w(x)$.

Eq. (23) indicates that lateral variations of mass moments, $\prod(P_L)$, are balanced by lateral variations of moments related to bending stresses. $\prod(P_L)$ can be calculated from the initial model geometry and associated densities (see Appendix A). $\prod(P_L)$ can further be expressed as a third-order polynomial in $h_{ex} = St(x) - St(\text{lowland})$, which is the laterally varying height of the topography. Therefore,

$h_{ex} = 0$ in the lowland of the model and $h_{ex} = h_e$ in the plateau (Fig. 4). We only have to consider powers of h_{ex} on the order of 2 and 3 since lower powers will disappear due to the second derivative of $\prod(P_L)$ in eq. (23):

$$\Pi(P_L) = h_{ex}^3 A + h_{ex}^2 B + ... \tag{24}$$

The coefficients A and B depend on the densities and geometrical parameters of the model configuration and are derived in Appendix A. We assume that initially $\prod(\sigma_{xx}^b)$ is non-zero only in the transition zone between lowland and plateau, and thus its polynomial form should include roots at $h_{ex} = 0$ and $h_{ex} = h_e$:

$$\Pi(\sigma_{xx}^b) = J\,h_{ex}\,[h_{ex} - h_e]\,[h_{ex} - K], \tag{25}$$

where J and K are unknown coefficients. Substituting eqs (24) and (25) into eq. (23) and comparing the terms on both sides of the equation yields

$$\begin{aligned} J &= A \\ K &= h_e - B/A. \end{aligned} \tag{26}$$

Characteristic values of σ_{xx}^b can then be estimated from $\prod(\sigma_{xx}^b)$ by (e.g. Turcotte & Schubert 2014; Medvedev 2016)

$$\sigma_{xx}^b \approx \pm\frac{6\Pi(\sigma_{xx}^b)}{ERT^2}, \tag{27}$$

where ERT is the effective rheological thickness discussed in Section 2.2. Eq. (27) applies to beams with uniform rheology and estimates maximum bending stresses at the upper and lower boundaries of the beam. In the lithosphere the rheology varies with depth and the bending regions are typically not limited by two sharp boundaries so that eq. (27) provides an upper limit for the bending stress. We will quantify values of bending stresses for a reasonable range of values of ERT. The horizontal deviatoric stress due to bending, τ_{xx}^b, can be approximated as half of the total bending stress (eq. (8))

$$\tau_{xx}^b \approx \frac{\sigma_{xx}^b}{2} \approx \pm\frac{3\Pi(\sigma_{xx}^b)}{ERT^2}. \tag{28}$$

The values of τ_{xx}^b vary laterally since $\prod(\sigma_{xx}^b)$ varies laterally due to its dependence of h_{ex} (Fig. 5a). The main uncertain parameters are the values of $w(x)$ and ERT and, therefore, we calculate maximum values of τ_{xx}^b for a range of reasonable values of $w(x)$ and ERT (Fig. 5b). The results show that maximum values of τ_{xx}^b are between 150 and 300 MPa corresponding to differential stresses approximately between 300 and 600 MPa. We will show that such maximum values for τ_{xx}^b and for associated differential stresses are in broad agreement with the results of the performed 2-D thermo-mechanical numerical simulations.

3 GPE VARIATION BETWEEN TIBETAN PLATEAU AND INDIAN LOWLAND

The structure and density distribution of the Tibetan plateau have been extensively investigated by mostly 2-D and some 3-D geophysical surveys based on land campaigns (e.g. Tilmann *et al.* 2003), satellite observations (e.g. Shin *et al.* 2015) and joint approaches (e.g. Basuyau *et al.* 2013). Such and other geophysical data sets, together with sparse thermal constraints as well as geological and petrological information, have been regularly used to construct models and geodynamic evolution scenario of the Tibetan plateau at various scales and levels of complexity (e.g. Dewey *et al.* 1988; Avouac & Tapponier 1993; Chemenda *et al.* 2000; Liu & Yang 2003; Beaumont *et al.* 2004; Zhao *et al.* 2010; Vozar *et al.* 2014; Baumann & Kaus 2015; Tunini *et al.* 2016).

For the current study we use two density fields to calculate the spatial variation of GPE between the Tibetan plateau and the Indian lowland, namely the density field from the CRUST1.0 data set (http://igppweb.ucsd.edu/~gabi/rem.html; Fig. 2) and the best-fit, *in situ* observation-constrained density field of Hetényi *et al.* (2007, their Fig. 6; Fig. 3a). The location of the density profile of Hetényi *et al.* (2007) corresponds to the blue solid line in Fig. 2(a). For the CRUST1.0 data, values of GPE were calculated using eqs (6) and (13) assuming a compensation depth, Sb, at 100 km. The calculated values of GPE first decrease in the region of the Indian foreland basin and then considerably increase with the increase of the topography along profiles from India towards the Tibetan plateau (Fig. 2). Values of ΔGPE between the Indian foreland region and the adjacent Tibetan plateau are *ca.* 10×10^{12} N m^{-1} (Fig. 2b). The considerable increase of topography between the Indian foreland and the Tibetan plateau occurs within a narrow region of *ca.* 100 km (Fig. 2c). The density field of Hetényi *et al.* (2007) provides an even larger ΔGPE of *ca.* 12×10^{12} N m^{-1} between the Indian foreland region and the adjacent Tibetan plateau (Fig. 3b). In contrast to the profile of ΔGPE resulting from the CRUST1.0 data, the ΔGPE resulting from the model of Hetényi *et al.* (2007) shows a smaller decrease of ΔGPE around the Indian foreland region (-200 km $< X < 0$ km in Fig. 3b) but higher ΔGPE around the adjacent Tibetan plateau (50 km $< X < 400$ km in Fig. 3b). The lithostatic pressure, P_L, at 100 km depth varies along the profile for both the CRUST1.0 and the Hetényi *et al.* (2007) model indicating that the depth of 100 km is not a level of local isostasy. The lateral variation of P_L and, hence, P_O indicates either non-zero deviatoric stresses or the influence of the flexural rigidity of the lithosphere (eq. (22)) in the region of the topographic increase which likely could be related to bending associated with the Indian foreland basin. Both density models show an increase of P_L in the region of considerable topographic variation and hence significant lateral variation of crustal thickness. This deviation from local isostasy can be expected due to the flexural strength of the Indian crust, which is deflected and thrusted under the Tibetan crust. This regional compensation is well documented by gravity anomalies (e.g. Berthet *et al.* 2013; Hammer *et al.* 2013; Hetényi *et al.* 2016). In Section 6, we argue that this geodynamic regime prevails since at least 10 Ma (e.g. Lu *et al.* 2018).

4 NUMERICAL MODEL

4.1 2-D thermomechanical finite-difference model

The applied numerical algorithm is based on the finite-difference/marker-in-cell method (e.g. Gerya & Yuen 2003; Duretz *et al.* 2016). The governing equations for 2-D incompressible deformation of viscoelastoplastic material coupled with heat transfer and gravity are described in detail in Appendix B. The diffusive terms in the force balance equations and in the heat transfer equations are discretized on an Eulerian staggered grid while advection and rotation terms are treated explicitly on Lagrangian markers using a fourth order in space Runge–Kutta time integration (Duretz *et al.* 2016). The topography in the model is a material interface defined by a Lagrangian marker chain and this interface is displaced with the numerically calculated velocity field. With ongoing deformation, this marker chain needs to be locally remeshed, which is achieved by adding marker points in the deficient chain segments. The applied numerical mesh consists of 2000 nodes in the horizontal direction

(resolution of 600 m) and 750 nodes in the vertical direction (resolution of 413 m). The models were run with a Courant number of 0.45 and a maximum allowed time step of 0.1 Ma.

4.2 Model configuration

The model configuration is similar to the model configuration which has been used to derive the analytical relations between ΔGPE, F_x and bending moments (Section 2, Fig. 4). The corresponding thicknesses and model dimensions are given in Fig. 4. The initial geometry and density field generates a GPE difference between plateau and lowland of *ca.* 7×10^{12} N m^{-1} in agreement with published data (e.g. Molnar *et al.* 1993) and the density field of CRUST1.0 (Fig. 2). The initial crustal geometry corresponds to isostatic equilibrium if the topographic variation is related to the variation of the crust–mantle boundary (Moho), that is, the transition width in which the topography increases is identical to the width of the region in which the Moho deepens (Fig. 4). However, the study of Hetényi *et al.* (2007; Fig. 3) indicates that the topography increases over a distance of *ca.* 100 km while the Moho deepens over a distance of *ca.* 300 km (Fig. 3). Therefore, we vary the transition width of the Moho (M; Fig. 4) in the simulations. The topographic transition width is always 100 km, close to the observed value.

For the 2-D numerical simulations we use the flow law of wet quartzite (Kirby 1983) for the upper crust and of Maryland diabase (Carter & Tsenn 1987) for the lower crust (Table 1). For the mantle lithosphere and asthenosphere we use a combination of dislocation and diffusion creep (Hirth & Kohlstedt 2003) for dry olivine and Peierls creep (Goetze & Evans 1979, with formulation of Kameyama *et al.* 1999; see Appendix B and Table 1). The left, right and bottom boundaries are free slip boundaries and the top boundary is a stress free surface. There is no far-field shortening or extension applied to the lateral boundaries as we focus on the evolution of the topographic relief. The top and bottom boundaries for heat transfer are described by fixed temperatures with 0 °C at the top and 1350 °C at the bottom. The lateral boundaries are zero heat flow boundaries. The initial temperature field is at equilibrium and is computed using the thermal parameters listed in Table 1.

5 RESULTS

5.1 Fundamental impact of crustal stress magnitudes

We first show the fundamental impact of the crustal friction angle on the numerical results by comparing two representative simulations, the only difference being the friction angle of the crust, namely, $\theta = 10°$ (simulation 1) and $\theta = 0°$ (simulation 2; Fig. 6). We use here the friction angle as parameter to limit maximum stress magnitudes in the crust without any particular mechanical interpretation, such as high fluid pressure or the presence of weak faults in the crust. We use $M = 300$ km, since this configuration is presumably closest to the observed geometry of Fig. 3. The scope of this comparison is to show the general deformation behaviour of the numerical model, the associated stress magnitudes and stress distributions and the fundamental impact of crustal stress magnitudes on the overall deformation of the lithosphere. For $\theta = 0°$, the maximum shear stress is limited by the cohesion only so that maximum differential stress in the upper crust in simulation 2 was 10 MPa, that is, twice the maximum shear stress of 5 MPa. In the following, we refer to the left model domain with initially normal crustal thickness of 35 km as lowland, to the right model domain with an initial topography of

Table 1. Model parameters. For all materials, specific heat is 1050 J kg^{-1} K^{-1}, thermal expansion is 1×10^{-5} K^{-1}, compressibility is 1×10^{-11} Pa^{-1}, shear modulus is 2.5×10^{10} Pa and cohesion is 5 MPa. The friction angle of the mantle lithosphere is always 30°. For the mantle lithosphere and asthenosphere, a combination of dislocation, diffusion and Peierls creep is applied. For diffusion and Peierls creep only those parameters are displayed that are different from the ones for dislocation creep; non-specified parameters are the same as for dislocation creep.

|	Dislocation creep						
	A (Pa^{-n} s^{-1})	n	Q (kJ mol^{-1})	k (W m^{-1} K^{-1})	ρ_0 (kg m^{-3})	H_R (W m^{-3})	V (m^3)
Upper crust India	5.0717×10^{-18}	2.3	154	2.5	2800	1.4×10^{-6}	0
Upper crust Tibet	5.0717×10^{-18}	2.3	154	2.5	2800	0.2×10^{-6}	0
Lower crust	3.2×10^{-20}	3.0	276	2.1	2800	0.2×10^{-6}	0
Mantle lithosphere	1.1×10^{-16}	3.5	530	3.0	3300	0	11×10^{-6}
Asthenosphere	1.1×10^{-16}	3.5	530	3.0	3250	0	11×10^{-6}
	Diffusion creep						
				d (m)	m		
Mantle lithosphere	1.5×10^{-15}	1	375	10^{-3}	3		9×10^{-6}
Asthenosphere	1.5×10^{-15}	1	375	10^{-3}	3		9×10^{-6}
	Peierls creep						
				A_p (s^{-1})	σ_p (Pa)	γ	
Mantle lithosphere			540	5.7×10^{11}	8.5×10^9	0.1	
Asthenosphere			540	5.7×10^{11}	8.5×10^9	0.1	
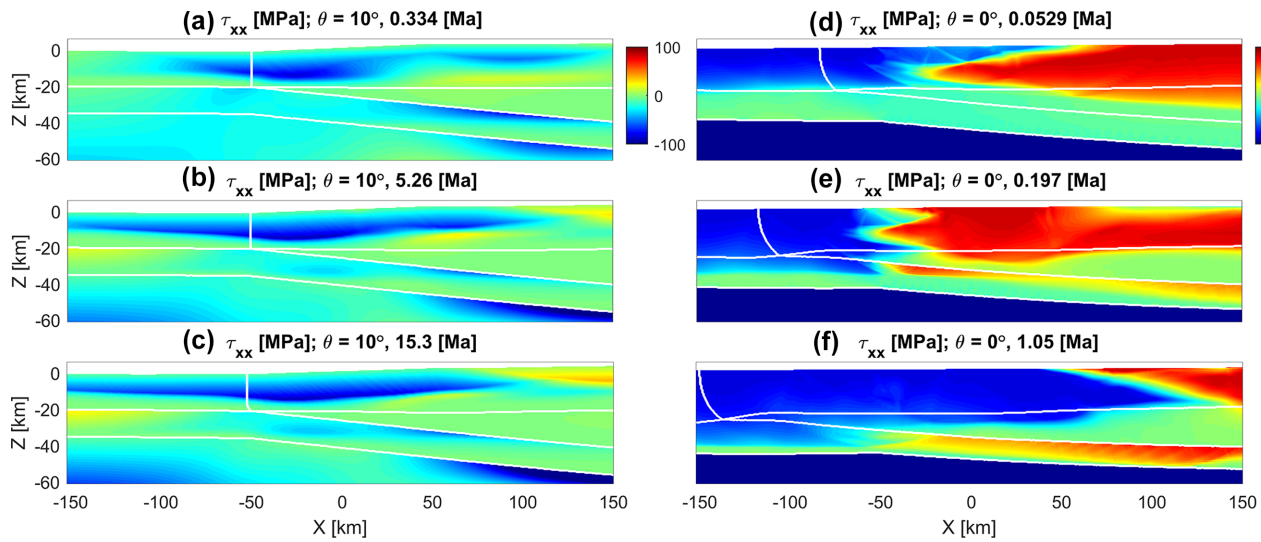
Figure 7. Enlargements of the colour plots of Fig. 6 for three different times for simulation 1 with a friction angle in the crust of 10° (a–c) and simulation 2 with 0° (d–f), both for $M = 300$ km. Negative values indicate compression, positive ones extension and the legends at the top right of the two columns (a–c and d–f) apply to the entire column. The region of the crust around the transition zone is shown. Times in million years (Ma) indicate the duration of the simulations. For a friction angle of 0° (d–f) the absolute magnitude of τ_{xx} is controlled by the cohesion of 5 MPa. The vertical white line, initially at $X = -50$ km, indicates the lateral flow of the crust.

5 km as plateau, and to the central model domain with an initially laterally varying crustal thickness as transition zone.

The stress distribution in the lithosphere is profoundly different for simulations 1 and 2 (Fig. 6). In simulation 1, high horizontal deviatoric stresses, τ_{xx}, are generally concentrated around the transition zone in the upper region of the mantle lithosphere and in the upper crust (Figs 6a–c). The lowland is under compression (negative deviatoric stress) and the plateau under extension (positive deviatoric stresses). Absolute maximum values of deviatoric stress in the lowland and plateau are similar and in the order of 100 MPa. Below the Moho in the mantle lithosphere, between $X = 0$ and 200 km, compressive stresses are directly above extensive stresses. This stress pattern indicates a region of bending where the upper region of the bending area is compressed, the lower region is extended and between the two regions is a neutral level with zero stress. This neutral level may be associated with the reference level $w(x)$ in the

analytical bending results of Section 2.3. The bending region is restricted to the transition zone, supporting the analytical assumption of eq. (25). In simulation 2 significant stresses occur only in the upper region of the mantle lithosphere in the transition zone and lowland (Figs 6d–f). Stress magnitudes in the mantle lithosphere in simulation 2 are locally more than twice the stresses in the mantle lithosphere in simulation 1. The higher bending stresses in simulation 2 are consistent with the analytical results of Section 2.3 which predict higher stresses for smaller values of ERT. The ERT of simulation 2 is thinner than the one of simulation 1 because crustal levels do not contribute to ERT in simulation 2. The absolute maximum magnitudes of 100–250 MPa for the deviatoric stresses due to bending agree also with rheology-independent analytical predictions (Fig. 5). The ERT of the mantle lithosphere in the transition zone of simulation 2 is between 40 and 50 km in agreement with values assumed in Fig. 5.
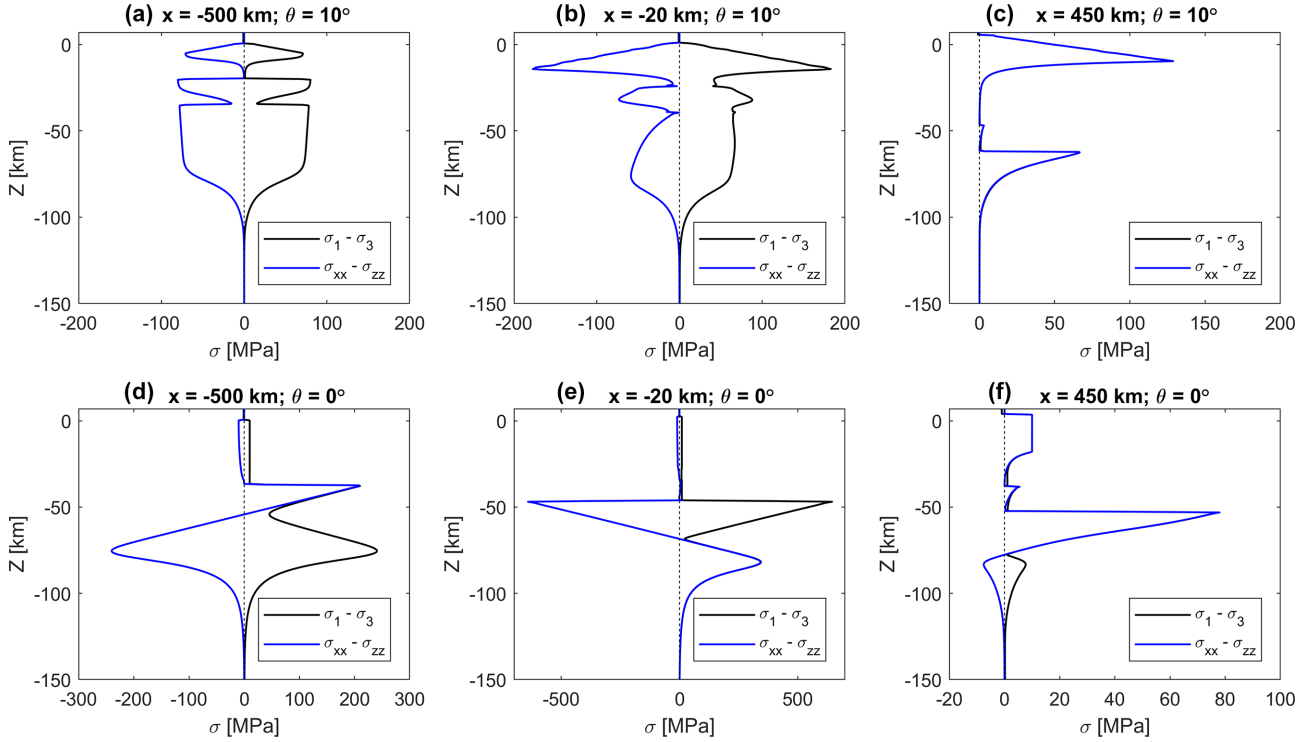
Figure 8. (a–c) Three vertical profiles of $\sigma_1 - \sigma_3$ and $\sigma_{xx} - \sigma_{zz}$ for simulation 1 ($\theta = 10°$ and $M = 300$ km) at ~15 Ma (Fig. 6c) in the lowland at $X = -500$ km (a), the transition zone at $X = -20$ km (b) and in the plateau at $X = 450$ km (c). See Fig. 6(c) for the horizontal X-position of the three profiles. (d–f) Three vertical profiles of $\sigma_1 - \sigma_3$ and $\sigma_{xx} - \sigma_{zz}$ for simulation 2 ($\theta = 0°$ and $M = 300$ km) at ~1 Ma (Fig. 6f) in the lowland at $X = -500$ km (d), the transition zone at $X = -20$ km (e) and in the plateau at $X = 450$ km (f). See Fig. 6(f) for the horizontal X-position of the three profiles.

In the upper crust of simulation 1, the transition between compressive and extensive regions occurs at the location where the initial topography reached the plateau height (Figs 7b and c). The upper crust with significant topographic slope is under compression. In simulation 2 the topography is essentially flat after 1 Ma but the transition between compression and extension occurs approximately at the same location as in simulation 1 (Figs 7d–f). Generally, lateral flow of material induced by GPE variations is not uniform with depth and the crust flows laterally towards the lowland while stronger levels of the mantle lithosphere essentially do not flow (material flow is indicated by initially vertical white lines in Fig. 7).

For simulation 1 at 15.3 Ma, vertical profiles of $\sigma_1 - \sigma_3$ and $\sigma_{xx} - \sigma_{zz}$ have been calculated in the lowland (Fig. 8a), in the transition zone (Fig. 8b) and in the plateau (Fig. 8c; see also Fig. 6c). By definition, values of $\sigma_1 - \sigma_3$ are always positive whereas values of $\sigma_{xx} - \sigma_{zz}$ are negative for compression and positive for extension. The lithosphere in the lowland is under compression and absolute values of $\sigma_1 - \sigma_3$ and $\sigma_{xx} - \sigma_{zz}$ are essentially identical which indicates negligible shear stresses, eq. (9), and negligible bending stresses since stresses do not change sign along the vertical profile. The same applies to stress profiles in the plateau (Fig. 8c) but stresses there are extensive and values of $\sigma_{xx} - \sigma_{zz}$ are positive. In the transition zone, absolute values of $\sigma_1 - \sigma_3$ and $\sigma_{xx} - \sigma_{zz}$ are not everywhere similar and in some depth the values of $\sigma_{xx} - \sigma_{zz}$ are nearly zero while corresponding values of $\sigma_1 - \sigma_3$ are significant with *ca.* 50–70 MPa (Fig. 8b). The stress profiles for simulation 1 show that the stress state of the lowland and plateau is dominated by membrane stresses while in the transition zone both membrane and bending stresses are important. The largest stresses occur at the brittle-ductile transition in the upper crust in the transition zone

where $\sigma_1 - \sigma_3 \approx 185$ MPa (Fig. 8b). In the lowland, the nearly vertical domains of the $\sigma_1 - \sigma_3$ versus depth profile indicate a viscoelastic deformation and stresses did not reach the plastic yield strength.

For simulation 2, vertical profiles of $\sigma_1 - \sigma_3$ at ~1.05 Ma at the same horizontal positions (Figs 8d–f) are significantly different to the ones of simulation 1. In contrast to simulation 1, profiles of the absolute values of $\sigma_1 - \sigma_3$ and $\sigma_{xx} - \sigma_{zz}$ vary significantly in the lowland, transition zone and plateau because values of $\sigma_{xx} - \sigma_{zz}$ change their sign along vertical profiles. This sign change is associated with significant bending stresses (Fig. 6f). Maximal values of $\sigma_1 - \sigma_3$ are *ca.* 645 MPa and occur in the transition zone at the top of the mantle lithosphere (Fig. 8e). Results of simulation 2 show that for a weak crust the deformation of the mantle lithosphere is dominated by bending and values of $\sigma_1 - \sigma_3$ reach several hundreds of MPa due to the reduced ERT of the lithosphere.

5.2 Accuracy of numerical models and applicability of analytical stress estimates

To evaluate the accuracy of the numerical results and to compare the analytical predictions of Section 2.2 with numerical results we calculate values of $\bar{\sigma}_{xx}$, F_x and GPE by vertical integration of the numerically calculated stresses and the model density field for both simulations 1 and 2 (Fig. 9). Representative results are shown for both simulations at *ca.* 8 Ma. Horizontal profiles of F_x, GPE and $\bar{\sigma}_{xx}$ are plotted by subtracting the leftmost values of F_x, GPE and $\bar{\sigma}_{xx}$ from all values of F_x, GPE and $\bar{\sigma}_{xx}$ (Figs 9a and c). As predicted by the analytical thin-sheet results (eq. 10), $\bar{\sigma}_{xx}$ is constant along the entire model (Figs 9a and c). Horizontal profiles
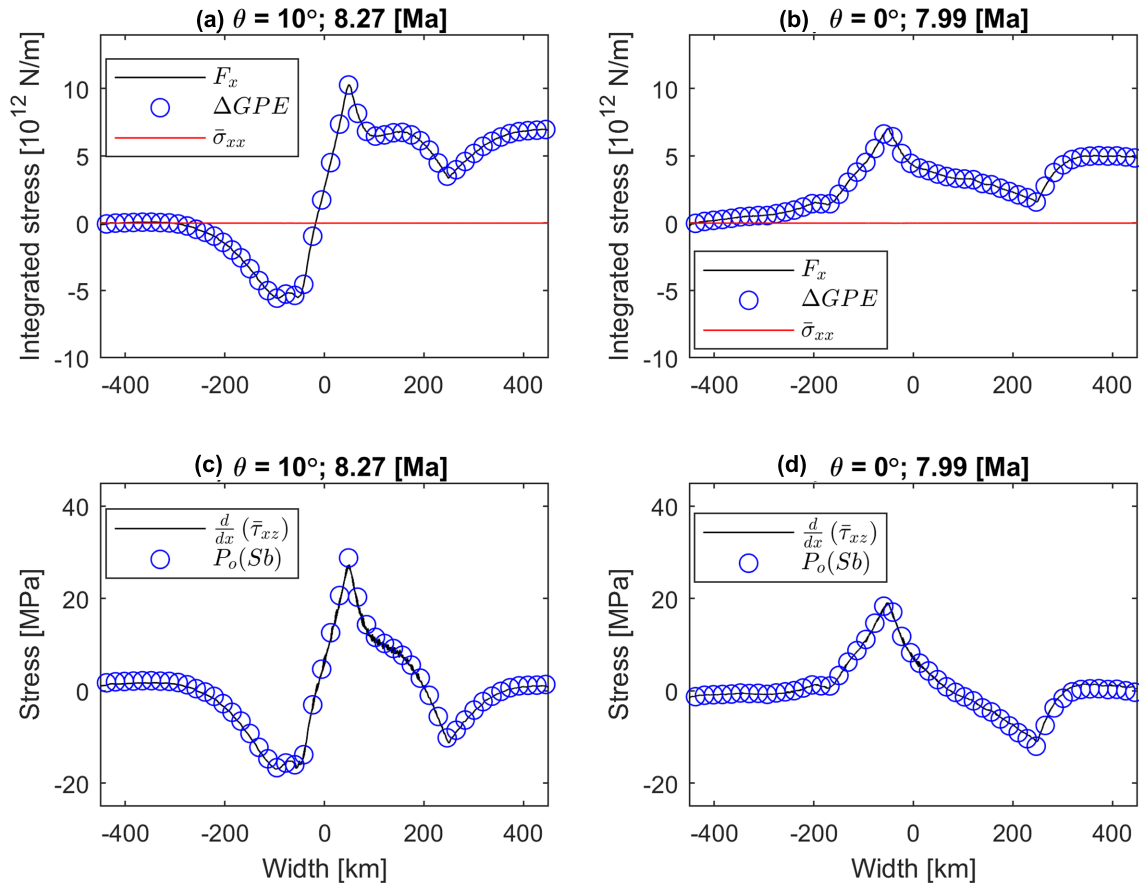
Figure 9. (a–c) Horizontal profiles of $\bar{\sigma}_{xx}$, F_x and ΔGPE calculated from the numerical simulations 1 (a) and from simulation 2 (c) at ~8 Ma. From all three quantities, the leftmost value is subtracted so that the quantities are zero at the left side of the plot. (b and d). Horizontal profiles of tectonic pressure, $P_O = P - P_L$, at the model bottom, Sb, and horizontal gradient of vertically integrated shear stress, $d\bar{\tau}_{xz}/dx$, calculated from the numerical simulations 1 (b) and 2 (d).

of F_x, calculated by numerically computed stresses, and profiles of ΔGPE, calculated by model densities, match along the entire model, demonstrating the correctness of the calculated stresses for the corresponding density fields (see eqs 14 and 15). The agreement of the horizontal profiles of F_x and GPE indicates that the simple analytical relations, which are independent on rheology, apply to considerably heterogeneous stress fields in the lithosphere. For simulation 1, values of ΔGPE vary strongly around the transition zone but values of F_x nevertheless correspond to values of ΔGPE. Maximum values of ΔGPE are *ca.* 10×10^{12} N m^{-1} and values in the right region of the plateau settle to *ca.* 7×10^{12} N m^{-1} (Fig. 9a). These values and the lateral variation of ΔGPE are close to values calculated from natural density fields (Fig. 3b). In contrast, for simulation 2 the profile of ΔGPE is significantly different, especially around the transition zone where values of ΔGPE are already of the same order as ΔGPE values in the plateau (Fig. 9c). The numerical results also show that the bottom of the model domain is not a level of local isostasy because values of P are not identical to P_L so that the tectonic pressure, $P_O = P - P_L$, varies along the model bottom (Figs 9b and d). As predicted by the analytical thin-sheet results (eq. (19)), the value of P_O at the model bottom is close to the numerically calculated value of $d\bar{\tau}_{xz}/dx$ (Figs 9b and d). The reason for the non-zero tectonic pressure at the model bottom is the flexural strength of the upper level of the lithosphere where the associated bending stresses are responsible for the deviation of the lithosphere from the local isostasy state (eq. (22)). For simulation 1 values of

$P_O(Sb)$ are close to zero on both model sides away from the transition zone because there the model domain is close to local isostasy. The largest deviation from local isostasy is around the transition zone with values of $P_O(Sb)$ close to 30 MPa. To the left and right of this maximum the values of $P_O(Sb)$ are negative with magnitudes as low as -20 MPa (Fig. 9b). The relative lateral variation of $P_O(Sb)$ in simulation 1 is similar to the pressure variation associated with the density fields of CRUST1.0 and Hetényi *et al.* (2007; Fig. 3c). The absolute magnitudes of $P_O(Sb)$ are slightly smaller in the numerical simulations. This is expected since the natural density field is only 100 km deep whereas the density field of the numerical simulation is 300 km deep and in such larger depth the deviation from local isostasy is presumably smaller. For simulation 2 the lateral variation of $P_O(Sb)$ is considerably different to the one of simulation 1 (Fig. 6f).

5.3 Crustal stress magnitudes required to maintain topographic relief

To determine the minimum crustal stress magnitude required to maintain the topographic relief between Indian lowland and Tibetan plateau for *ca.* 10 Ma, we performed a series of simulations for the model configuration shown in Fig. 4. We varied systematically two parameters, namely the friction angle of the crust, $\theta = 0°$, $3°$, $6°$, $10°$ and $30°$, and the Moho transition width, $M = 50$, 100, 200 and 300 km. The results of all the performed simulations show
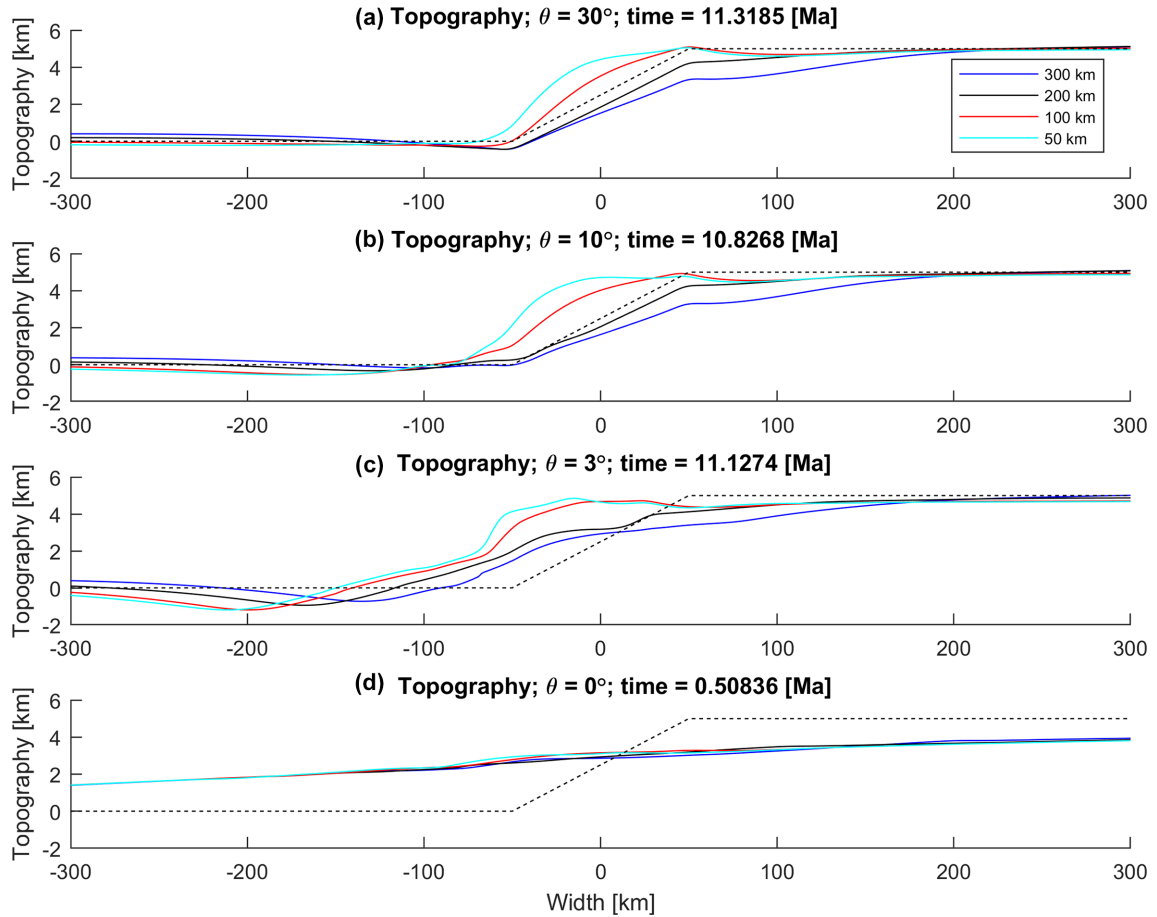
Figure 10. Lateral variation of topography for simulations with different friction angle in the crust, θ, and different initial Moho transition zone widths, M (distance in legend in panel a applies to all panels). The topography is given for the same time (in Ma) for simulations with the same θ but times differ for simulations with different θ. The dashed black line in all four panels indicates the initial topography.

that both θ and M have a significant impact on the topography evolution (Fig. 10). The collapse, or lateral flow, of the topographic relief reaches the maximum value for $M = 50$ km, whereas it is minimal for $M = 300$ km. For $\theta = 30°$ and $10°$ the width of the topographic transition zone is essentially stable and tends to the corresponding values of M after *ca.* 11 Ma (Figs 10a and b). For $\theta = 3°$ the width of the topographic transition zone has essentially doubled at *ca.* 11 Ma when compared to the corresponding initial value of M (Fig. 10c). For $\theta = 0°$ there is no more topographic transition zone after already *ca.* 0.5 Ma (Fig. 10d). The results for $\theta = 0°$ show that maximum values of $\Delta\sigma$ of *ca.* 10 MPa in the crust are unable to maintain the topographic relief between lowland and plateau for as little as 0.5 Ma. We focus on the evolution of topography with time for simulations with $\theta = 10°$, $3°$ and $0°$ and for $M = 300$ km (Fig. 11). For $\theta = 10°$ the width of the topographic transition zone is more or less stable in the horizontal direction within the displayed 15 Ma (Fig. 11a). Also, no significant foreland basin with negative topography is formed in the lowland (Fig. 11a). In contrast, for $\theta = 3°$ the width of the topographic transition zone widens significantly within 15 Ma (Fig. 11b). Furthermore, a basin with a depth of more than 500 m subsidence develops in the lowland and this basin migrates more than 100 km towards the foreland within 15 Ma (Fig. 11b). For $\theta = 0°$ there is essentially no difference anymore between plateau and lowland already after 1 Ma (Fig. 11c).

We compare all the performed simulations with different θ and M by calculating for each simulation the maximum differential stress, $\Delta\sigma_{max}$, at $X = 0$ km which occurred in the upper crust within the entire simulation duration (Fig. 12a). Fig. 12(a) presents values of the maximum differential stress reached within the upper crust for a range of θ and M. Values of $\Delta\sigma_{max}$ increase from 10 to *ca.* 220 MPa for increasing values of θ, whereas they are essentially independent of M (Fig. 12a). The maximum values of the horizontal velocity at the surface at $X = 0$, V_{x0}, for each simulation decrease with increasing θ (Fig. 12b). For $\theta < 10°$ the decrease of V_{x0} with increasing θ is significant and essentially independent of M. However, for $\theta \geq 10°$ the V_{x0} essentially does not decrease anymore with increasing θ, but the decrease depends on M, whereby larger values of M correspond to smaller V_{x0} (Fig. 12b). The results show that for a given M an increase in θ from $0°$ to $10°$ causes an increase in $\Delta\sigma_{max}$ which decreases V_{x0} and, hence, significantly help to maintain plateau relief. An increase in θ from $10°$ to $30°$ still causes an increase in $\Delta\sigma_{max}$ but this stress increase does not significantly decrease V_{x0}. The plateau is most stable, that is, V_{x0} is smallest, for $M = 300$ km which is closest to the observed geometry (Fig. 3a). In the simulations with $\theta = 10°$ and $M = 300$ km values of $\Delta\sigma_{max}$ are *ca.* 180 MPa and the systematic results (Fig. 12) indicate that such stress levels are minimum stress levels that are required in the upper crust to support the relief of the plateau for a duration on the order of 10 Ma.
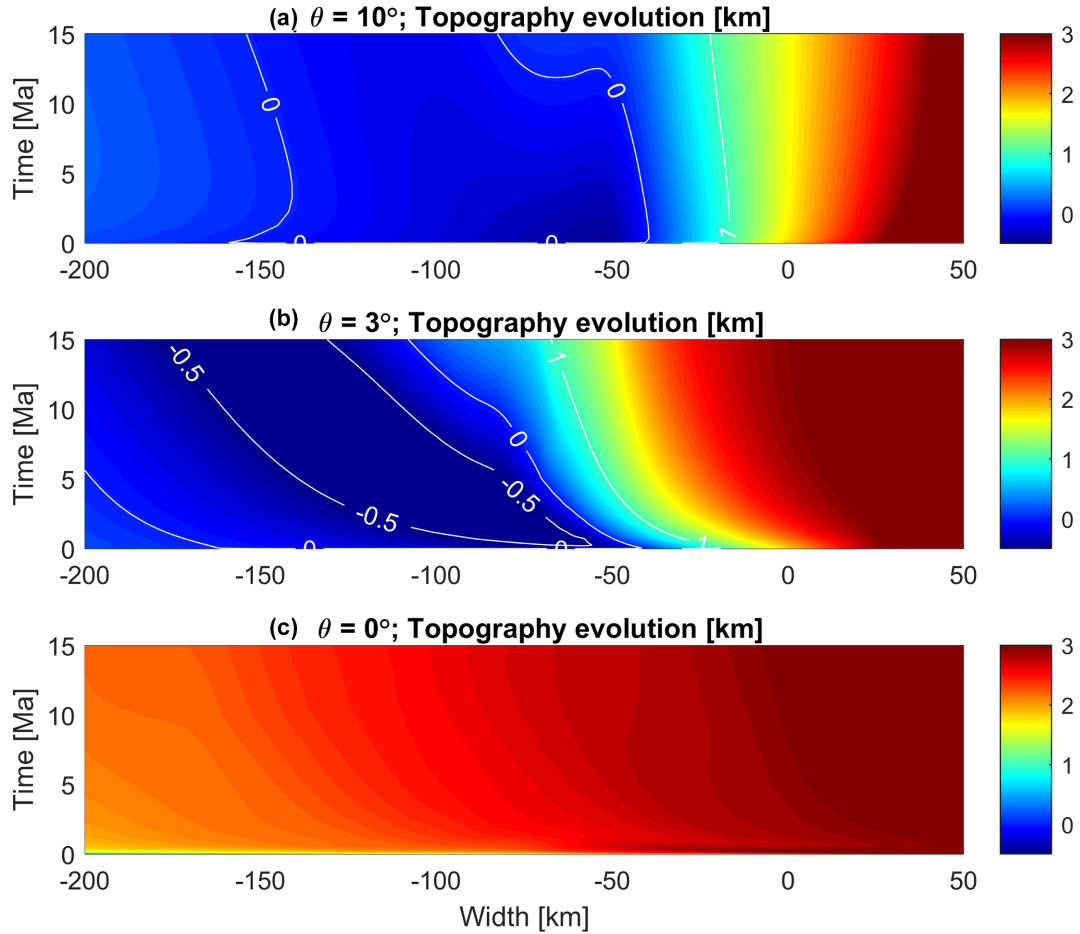
Figure 11. Colour plot of the evolution of topography (in km) with time for three simulations all with $M = 300$ km but different crustal friction angles, θ, of $10°$ (a), $3°$ (b) and $0°$ (c). In panel (a) and (b), white contour lines indicate the topography of -0.5, 0 and 1 km.

For the simulation with $\theta = 10°$ and $M = 300$ km the vertical integral of the differential stress across the lithosphere, $\overline{\Delta\sigma}_L$, varies significantly horizontally but insignificantly with time (Fig. 13a). The maximal values of $\overline{\Delta\sigma}_L$ occur in the transition zone and are *ca.* 7.5×10^{12} N m^{-1}. The relative contribution of the stresses in the crust to the stresses in the entire lithosphere is quantified by the ratio of the vertically integrated differential stress across the crust, $\overline{\Delta\sigma}_C$, to $\overline{\Delta\sigma}_L$. In the transition zone the values of $\overline{\Delta\sigma}_C/\overline{\Delta\sigma}_L$ are >0.3 and in the right side of the plateau even >0.5 so that in these regions the contribution of the crust to the integrated lithospheric stress is significant (Fig. 13b). In some regions of the lowland, values of $\overline{\Delta\sigma}_C/\overline{\Delta\sigma}_L$ decrease to *ca.* 0.1 (Fig. 13b). The results show that the contribution of the crust to the vertically integrated differential stresses in the lithosphere varies significantly horizontally. For comparison, for the simulation with $\theta = 3°$ and $M = 300$ km maximal values of $\overline{\Delta\sigma}_L$ also occur around the transition zone but are slightly larger reaching up to *ca.* 8.5×10^{12} N m^{-1} (Fig. 13c). Values of $\overline{\Delta\sigma}_C/\overline{\Delta\sigma}_L$ can locally also be larger than 0.3 (Fig. 13d).

For $\theta = 10°$ and $M = 300$ km the maximum differential stress, $\Delta\sigma_{max}$, in the upper crust is *ca.* 185 MPa (Fig. 14a) while for $\theta = 3°$ and $M = 300$ km it is *ca.* 80 MPa (Fig. 14d). For both simulations, maximum values of $\Delta\sigma_{max}$ occur around the transition zone (Figs 14a and d). In the lower crust, values of $\Delta\sigma_{max}$ are more or less the same for $\theta = 10°$ and $3°$ and are *ca.* 120 MPa (Figs 14b and e). In the mantle lithosphere, values of $\Delta\sigma_{max}$ are larger for $\theta = 3°$ reaching >500 MPa (Fig. 14f) while for $\theta = 10°$ maximum

values of $\Delta\sigma_{max}$ are *ca.* 350 MPa (Fig. 14c). For $\theta = 3°$, the high stress values are due to bending of the relatively thin (<50 km) and strong upper level of the mantle lithosphere; in agreement with analytical bending results (Fig. 5).

6 DISCUSSION

The present day ΔGPE in the transition zone between Indian lowland and Tibetan plateau is about 10 to 12×10^{12} N m^{-1} (Fig. 3b). If averaged over a 100 km thick lithosphere, these ΔGPE variations imply average values of $\Delta\sigma_{xx}^d$ between 100 and 120 MPa and average values of $\Delta\tau_{xx}$ between 50 and 60 MPa (eq. 15). Assuming that absolute values of $\tau_{xx} = \Delta\tau_{xx}/2$ yields typical absolute values of τ_{xx} between 25 and 30 MPa. Due to the pressure-sensitive yield stress and the temperature-dependent viscosity of rocks, the stresses cannot be constant with depth. Assuming that the load-bearing levels in the lithosphere have a cumulative ERT of one half to one third of the total lithospheric thickness of 100 km implies that values of τ_{xx}^* are between 50 and 90 MPa (eq. 17; assuming $\tau_{xx}^* = \Delta\tau_{xx}^*/2$). These stress magnitudes are in broad agreement with values of $\sigma_1 - \sigma_3$ occurring in the high-stress regions in the numerical simulations (Figs 6 and 14). However, the analytical and numerical results indicate that stresses in the lithosphere can be locally considerably larger if bending is significant (Figs 6 and 14).
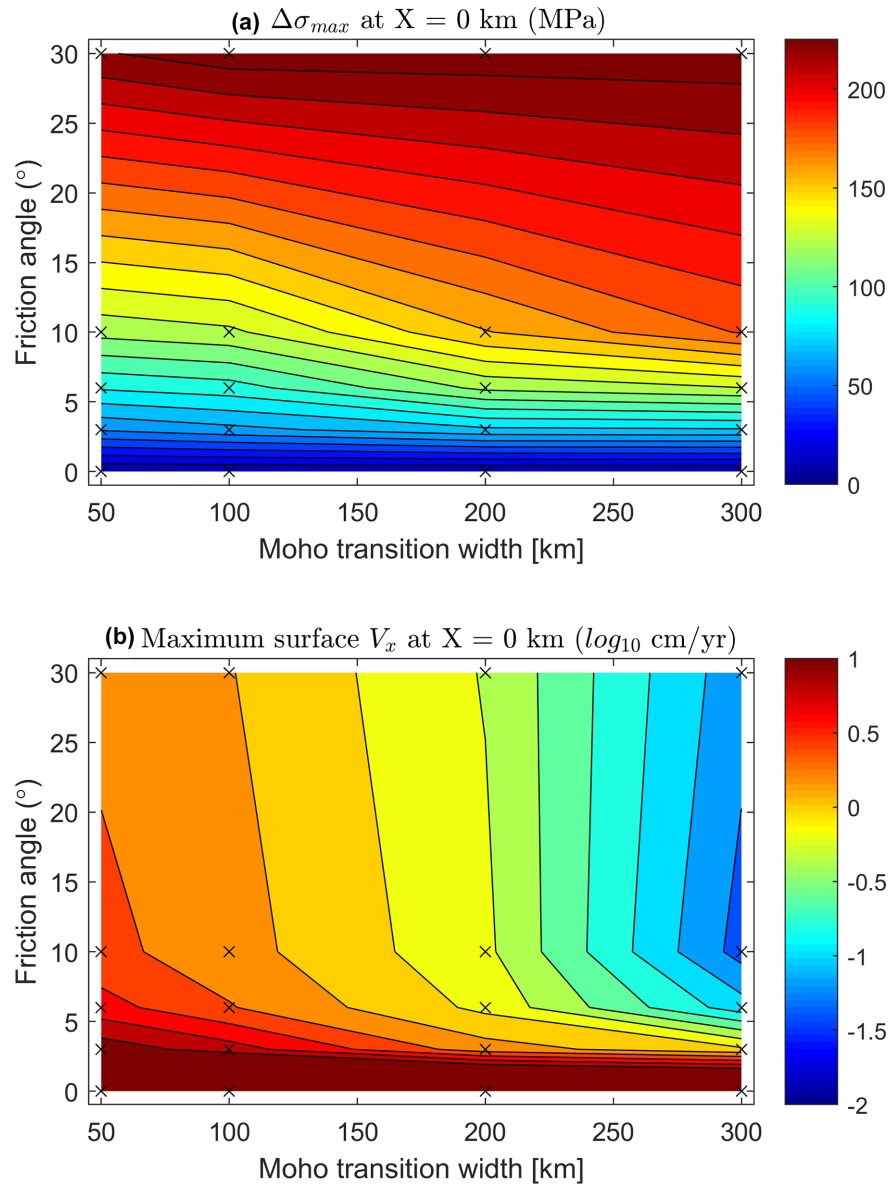
Figure 12. Maximum differential stress (in MPa) in the upper crust (a) and maximum horizontal velocity at the surface (b) at *X*-position $= -50$ km for simulations with different crustal friction angle, θ, and different Moho transition width, *M*. Stress values in panel (a) for specific values of θ and *M* represent the maximum value at some depth in the upper crust of the entire corresponding numerical simulation at the *X*-position $= -50$ km. Velocity values in panel (b) for specific values of θ and *M* represent the maximum value at the surface of the entire corresponding numerical simulation at the *X*-position $= -50$ km. The logarithm to the basis 10 of the velocity (in cm yr^{-1}) is displayed.

Allmann & Shearer (2009) report that the median of earthquake-based stress drop estimates of about 4 MPa does not vary significantly with seismic moment and within the top 45 km of the lithosphere. Our results indicate that median stress drop values of 4 MPa, corresponding to differential stress of *ca.* 8 MPa, cannot be representative for the absolute deviatoric stress magnitudes in a crust with lateral variations of *GPE* as observed between the Indian lowland and the Tibetan plateau. Absolute deviatoric magnitudes between one and two orders of magnitudes larger than 4 MPa are required to maintain the relief of the Tibetan plateau over geological spatial and time scales (Figs 6b and c). Stress magnitudes of several hundreds of MPa have also been reported from 3-D numerical simulations of the present-day India–Asia collision (Lechmann *et al.* 2014). Therefore, stress drop estimates of *ca.* 4 MPa represent most likely only a minor fraction of the total crustal deviatoric stress magnitude; at

least in a collisional setting mimicking the India–Himalaya–Tibet system. A possible explanation for the different stress estimates has been proposed by Nadeau & Johnson (1998) who argue that stresses on fault planes are strongly heterogeneous and that stresses around fault plane asperities with surface <1 m^2 can be locally very high, up to 2000 MPa, whereas the corresponding stress drop, which is averaged over the entire fault plane, is orders of magnitudes smaller and thus provides a stress drop between 1 and 10 MPa.

A key assumption for our estimates of crustal stress magnitudes is that the topography of the Tibetan plateau was relatively stable during the last 10 Ma. This assumption can be supported by a representative cross-section from India to Tibet (Figs 2 and 3) which is characterized by considerable underthrusting of Indian lower crust below Tibet (Hetényi *et al.* 2007; Nábělek *et al.* 2009). The underthrusted Indian lower crust is approximately horizontal along
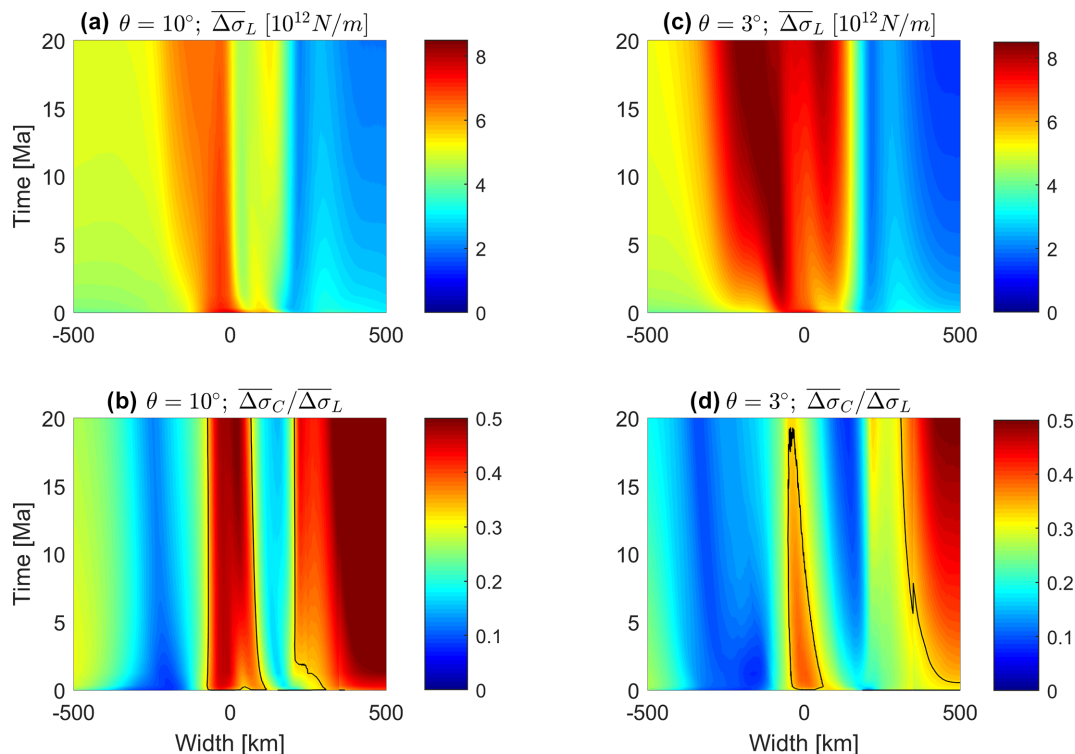
Figure 13. Evolution of vertically integrated differential stress with time for simulations with $M = 300$ km. Panels (a) and (b) show results for $\theta = 10°$, and panels (c) and (d) for $\theta = 3°$. Panels (a) and (c) show the evolution of the vertically integrated differential stress across the entire lithosphere, $\overline{\Delta\sigma}_L$. Panels (b) and (d) show the evolution of the ratio of vertically integrated differential stress across the crust to the vertically integrated differential stress across the entire lithosphere, $\overline{\Delta\sigma}_C/\overline{\Delta\sigma}_L$. The black contour line indicates a ratio of 1/3 and the orange–red domains indicate regions where the integrated crustal strength is larger than one third of the entire integrated lithospheric strength.

250 km below Tibet. Geophysical data indicates that this under-thrusting extends for at least *ca.* 1000 km along the strike of the central part of the Himalayas (Wittlinger *et al.* 2009). The geodetic and geological shortening rate across the Himalaya is *ca.* 2 cm yr^{-1}, so that the *ca.* 250 km underthrusting occurred over the last *ca.* 12.5 Ma. Assuming that the underthrusting was horizontal implies that there were no major vertical displacements during the last 12.5 Ma because otherwise the Indian lower crust would today not be horizontal over a length of 250 km. The absence of significant crustal-scale vertical displacements suggests that the topographic relief between India and Tibet and the more or less flat topography of southern Tibet likely existed for times on the order of 10 Ma. There is geological evidence, independent from the previously presented geophysical arguments, in support of Southern Tibet's high elevation since *ca.* 10 Ma or more. While the Tibetan plateau's uplift history has evolved from north to south (Molnar *et al.* 2010), several approaches point out that its elevation was close to 4000 m over geologically significant times. For the central part of the plateau, palaeoaltimetry suggests elevations higher than 4000 m since 35 ± 5 Ma (Rowly & Curie 2006). In a compilation, Harris (2006) argues that elevations in the southern part of the plateau have not changed since at least 15 Ma, and this time is pushed back locally as far as 28 Ma for an elevation of 5000 m (Xu *et al.* 2013). Thermochronologic, sedimentologic, oceanographic and palaeoclimatic studies suggest that rapid uplift of Southern Tibet started 20 Ma ago and reached the present elevation by 8 Ma (Harrison *et al.* 1992). Fielding (1996)

even argues for higher elevation than current prior to 8 Ma and its slow decrease during the late Cenozoic. Similar findings have been reported over Tibet and the Himalaya by Quade *et al.* (2011). Finally, cosmogenic nuclide exposure histories in southern and central Tibet, although measured on much shorter time scales, suggest very low erosion rates, less than 30 m Ma^{-1} (Lal *et al.* 2004). The above observations support our assumption that the Tibetan plateau and the present-day topographic relief can have existed for a duration of *ca.* 10 Ma.

The simulations show that crustal strength does not only affect the evolution of lowland-plateau transition zone width but also the formation of a sedimentary basin in the foreland. For $\theta = 3°$ maximum values of $\sigma_1 - \sigma_3$ in the upper crust are *ca.* 80 MPa (Fig. 14) and for $\theta = 3°$ a basin forms in the lowland with a depth between 0.5 and 1 km. This basin is steadily migrating away from the topographic relief. This is not the case in the Himalayan foreland, as the Ganges foreland basin is getting broader with time, but the deepest part remains close to the topographic front as a result of flexure (see map in Hetényi *et al.* 2016). This is witnessed by the accumulated lower, middle and upper Siwalik sedimentary units, studied in surface outcrops and boreholes (e.g. Sastri *et al.* 1971; Schelling 1992; Métivier *et al.* 1999). The situation is different at the Brahmaputra foreland basin in the east, where the very shallow sedimentary basin is explained by a different foreland lithosphere and seismotectonics (Hetényi *et al.* 2016; Diehl *et al.* 2017; Grujic *et al.* 2018).
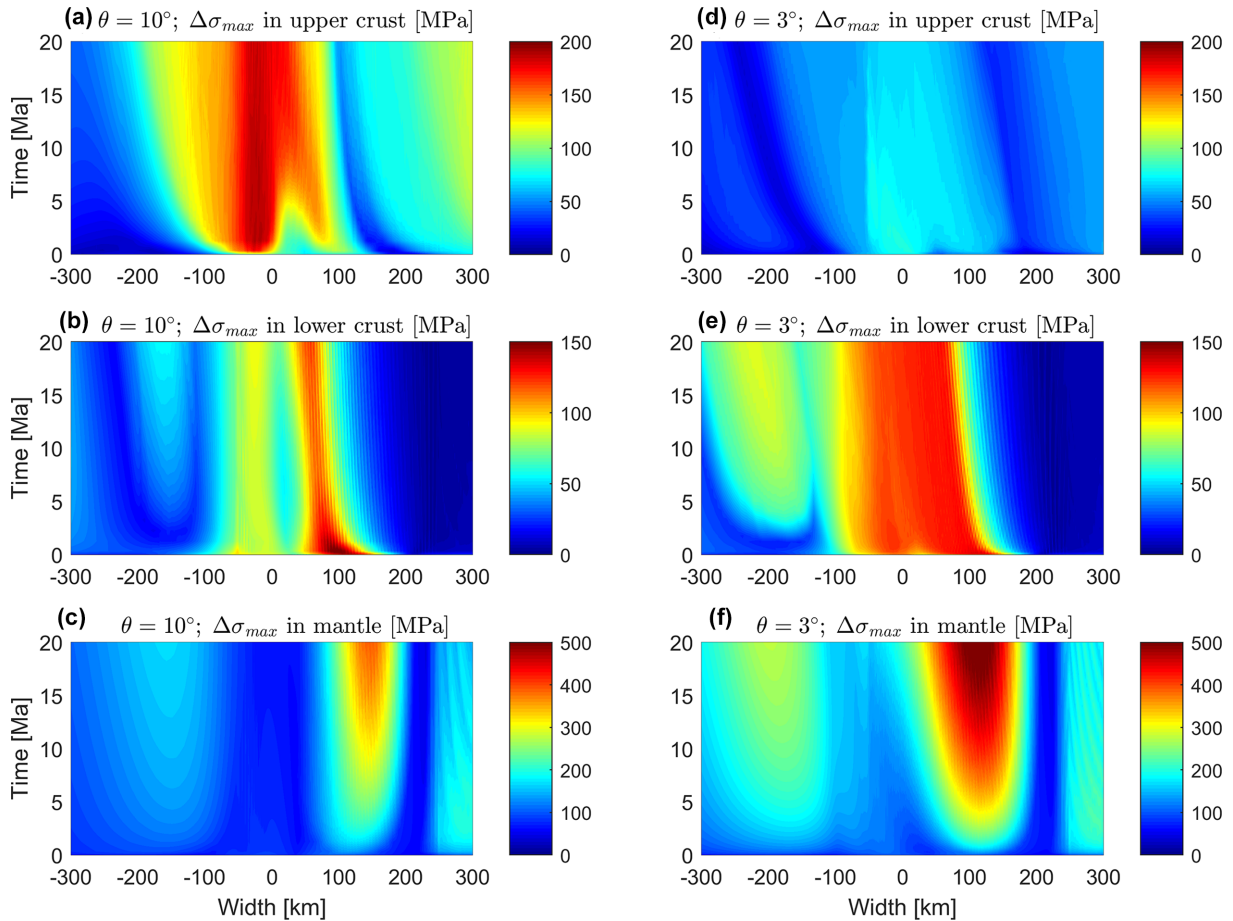
Figure 14. Evolution of maximum differential stresses, $\Delta\sigma_{max}$ (MPa), in the upper crust (a and d), the lower crust (b and e) and the mantle lithosphere (c and f) for simulations with $\theta = 10°$ (a–c) and $3°$ (d–f), both with $M = 300$ km. $\Delta\sigma_{max}$ indicates the maximum differential stress that occurred at a specific X-position and time within the respective model unit.

7 CONCLUSIONS

The numerical simulations show that maximum magnitudes of differential stress in the upper crust must be at least *ca.* 180 MPa to maintain the relief of the Tibetan plateau for a duration of *ca.* 10 Ma. The required crustal stress magnitudes are at least one order of magnitude larger than median earthquake-based stress drop estimates from seismology of *ca.* 4 MPa, corresponding to *ca.* 8 MPa differential stress. Analytical estimates of stress magnitudes based on lateral variation of *GPE* agree with stress magnitudes in the performed 2-D thermomechanical numerical simulations. We, therefore, argue that median stress drop estimates do not represent absolute stress magnitudes in the crust around the Tibetan plateau and that stress drop estimates are relative, and only represent a small fraction of the total crustal stress.

The performed simulations show that the contribution of depth-integrated crustal stress to the lithospheric depth-integrated stress varies significantly along profile between lowland and plateau. The results indicate that depth-integrated crustal stress in the region between lowland and plateau must be approximately equal to the depth-integrated stress of the mantle lithosphere in order to maintain the topographic relief of the Tibetan plateau.

The large-scale density heterogeneities between lowland and plateau can result in significant bending moments and large bending stresses in the rheologically stratified lithosphere. Analytical and numerical results show that the magnitudes of bending stresses

can be few hundreds of MPa. The magnitude of bending stresses strongly depends on the effective rheological thickness of the lithosphere. Therefore, the value of the crustal friction angle controls not only the stress magnitudes in the crust but also in the mantle lithosphere, because this friction angle controls the effective rheological thickness of the lithosphere. Smaller crustal stresses cause a smaller effective rheological thickness of the lithosphere, which in turn causes higher bending-related stresses in the mantle lithosphere.

Simple analytical relations between depth-integrated horizontal stresses, horizontal variations of depth-integrated shear stresses, tectonic pressure at the compensation depth, and bending stresses based on rheology-independent estimations from lateral *GPE* variations and integrated density moments are valid for highly variable stress fields calculated with 2-D numerical thermomechanical simulations considering viscoelastoplastic deformation. Therefore, these analytical relations are useful to estimate stress magnitudes in the lithosphere and to test the correctness and accuracy of numerical algorithms for modelling lithospheric deformation.

REFERENCES

Allmann, B.P. & Shearer, P.M., 2009. Global variations of stress drop for moderate to large earthquakes, *J. geophys. Res.,* **114.**

Andersen, T.B., Mair, K., Austrheim, H., Podladchikov, Y.Y. & Vrijmoed, J.C., 2008. Stress release in exhumed intermediate and deep earthquakes determined from ultramafic pseudotachylyte, *Geology,* **36,** 995–998.

Artyushkov, E., 1973. Stresses in lithosphere caused by crustal thickness inhomogeneities, *J. geophys. Res.,* **78,** 7675–7708.

Avouac, J.P. & Tapponnier, P., 1993. Kinematic model of active deformation in central Asia, *Geophys. Res. Lett.,* **20,** 895–898.

Basuyau, C., Diament, M., Tiberi, C., Hetényi, G., Vergne, J. & Peyrefitte, A., 2013. Joint inversion of teleseismic and GOCE gravity data: application to the Himalayas, *Geophys. J. Int.,* **193,** 149–160.

Baumann, T. & Kaus, B.J., 2015. Geodynamic inversion to constrain the non-linear rheology of the lithosphere, *Geophys. J. Int.,* **202,** 1289–1316.

Beaumont, C., Jamieson, R.A., Nguyen, M.H. & Medvedev, S., 2004. Crustal channel flows: 1. Numerical models with applications to the tectonics of the Himalayan–Tibetan orogen, *J. geophys. Res.,* **109.**

Behr, W.M. & Platt, J.P., 2014. Brittle faults are weak, yet the ductile middle crust is strong: Implications for lithospheric mechanics, *Geophys. Res. Lett.,* **41,** 8067–8075.

Berthet, T. *et al.*, 2013. Lateral uniformity of India Plate strength over central and eastern Nepal, *Geophys. J. Int.,* **195,** 1481–1493.

Beuchert, M.J. & Podladchikov, Y.Y., 2010. Viscoelastic mantle convection and lithospheric stresses, *Geophys. J. Int.,* **183,** 35–63.

Brudy, M., Zoback, M., Fuchs, K., Rummel, F. & Baumgärtner, J., 1997. Estimation of the complete stress tensor to 8 km depth in the KTB scientific drill holes: Implications for crustal strength, *J. geophys. Res.,* **102,** 18 453–18 475.

Burov, E.B., 2011. Rheology and strength of the lithosphere, *Mar. Pet. Geol.,* **28,** 1402–1443.

Burov, E.B. & Diament, M., 1995. The effective elastic thickness (Te) of continental lithosphere: what does it really mean?, *J. geophys. Res.,* **100,** 3905–3927.

Carter, N.L. & Tsenn, M.C., 1987. Flow properties of continental lithosphere, *Tectonophysics,* **136,** 27–63.

Cattin, R., Martelet, G., Henry, P., Avouac, J.P., Diament, M. & Shakya, T.R., 2001. Gravity anomalies, crustal structure and thermo-mechanical support of the Himalaya of central Nepal, *Geophys. J. Int.,* **147,** 381–392.

Chemenda, A.I., Burg, J.-P. & Mattauer, M., 2000. Evolutionary model of the Himalaya–Tibet system: geopoem: based on new modelling, geological and geophysical data, *Earth planet. Sci. Lett.,* **174,** 397–409.

Dewey, J.F., Shackleton, R.M., Chengfa, C. & Yiyin, S., 1988. The tectonic evolution of the Tibetan plateau, *Phil. Trans. R. Soc. Lond., A,* **327,** 379–413.

Diehl, T., Singer, J., Hetényi, G., Grujic, D., Giardini, D., Clinton, J. & Kissling, E., GANSSER Working Group, 2017. Seismotectonics of Bhutan: evidence for segmentation of the Eastern Himalayas and link to foreland deformation, *Earth planet. Sci. Lett.,* **471,** 54–64.

Duretz, T., Petri, B., Mohn, G., Schmalholz, S.M., Schenker, F.L. & Muntener, O., 2016. The importance of structural softening for the evolution and architecture of passive margins, *Sci. Rep.,* **6.**

England, P. & McKenzie, D., 1982. A thin viscous sheet model for continental deformation, *Geophys. J. R. astr. Soc.,* **70,** 295–321.

England, P. & Molnar, P., 2015. Rheology of the lithosphere beneath the central and western Tien Shan., *J. geophys. Res.: Solid Earth,* **120,** 3803–3823.

Fielding, E.J., 1996. Tibet uplift and erosion, *Tectonophysics,* **260,** 55–84.

Gerya, T., 2010. *Introduction to Numerical Geodynamic Modelling,* Cambridge Univ. Press.

Gerya, T.V. & Yuen, D.A., 2003. Characteristics-based marker-in-cell method with conservative finite-differences schemes for modeling geological flows with strongly variable transport properties, *Phys. Earth planet. Inter.,* **140,** 293–318.

Ghosh, A., Holt, W.E. & Flesch, L.M., 2009. Contribution of gravitational potential energy differences to the global stress field, *Geophys. J. Int.,* **179,** 787–812.

Ghosh, A., Holt, W.E., Flesch, L.M. & Haines, A.J., 2006. Gravitational potential energy of the Tibetan Plateau and the forces driving the Indian plate, *Geology,* **34,** 321–324.

Goetze, C. & Evans, B., 1979. Stress and temperature in the bending lithosphere as constrained by experimental rock mechanics, *Geophys. J. R. astr. Soc.,* **59,** 463–478.

Grujic, D., Hetényi, G., Cattin, R., Baruah, S., Benoit, A., Drukpa, D. & Saric, A., 2018. Stress transfer and connectivity between the Bhutan Himalaya and the Shillong Plateau, *Tectonophysics,* **744,** 322–332.

Hammer, P. *et al.*, 2013. Flexure of the India plate underneath the Bhutan Himalaya, *Geophys. Res. Lett.,* **40,** 4225–4230.

Hardebeck, J.L. & Okada, T., 2018. Temporal stress changes caused by earthquakes: a review, *J. geophys. Res.,* **123,** 1350–1365.

Harris, N., 2006. The elevation history of the Tibetan Plateau and its implications for the Asian monsoon, *Palaeogeogr. Palaeoclimatol. Palaeoecol.,* **241,** 4–15.

Harrison, T.M., Copeland, P., Kidd, W.S.F. & Yin, A., 1992. Raising Tibet, *Science,* **255,** 1663–1670.

Hetényi, G., 2014. To conserve or not to conserve (mass in numerical models), *Terra Nova,* **26,** 372–376.

Hetényi, G., Cattin, R., Brunet, F., Bollinger, L., Vergne, J., Nábělek, J.L. & Diament, M., 2007. Density distribution of the India plate beneath the Tibetan plateau: geophysical and petrological constraints on the kinetics of lower-crustal eclogitization, *Earth planet. Sci. Lett.,* **264,** 226–244.

Hetényi, G., Cattin, R., Vergne, J. & Nábělek, J.L., 2006. The effective elastic thickness of the India Plate from receiver function imaging, gravity anomalies and thermomechanical modelling, *Geophys. J. Int.,* **167,** 1106–1118.

Hetényi, G., Godard, V., Cattin, R. & Connolly, J.A.D., 2011. Incorporating metamorphism in geodynamic models: the mass conservation problem, *Geophys. J. Int.,* **186,** 6–10.

Hetényi, G. *et al.*, 2016. Segmentation of the Himalayas as revealed by arc-parallel gravity anomalies, *Sci. Rep.,* **6,** 33866.

Hirth, G. & Kohlstedt, D., 2003. Rheology of the upper mantle and the mantle wedge: a view from the experimentalists, *Inside Subduction Factory,* **138,** 83–105.

Hirth, G. & Tullis, J., 1994. The brittle-plastic transition in experimentally deformed quartz aggregates, *J. geophys. Res.: Solid Earth,* **99,** 11731–11747.

Jaquet, Y., Duretz, T. & Schmalholz, S.M., 2016. Dramatic effect of elasticity on thermal softening and strain localization during lithospheric shortening, *Geophys. J. Int.,* **204,** 780–784.

Jaquet, Y. & Schmalholz, S.M., 2018. Spontaneous ductile crustal shear zone formation by thermal softening and related stress, temperature and strain rate evolution, *Tectonophysics,* **746,** 384–397.

Jeffreys, H., 1959. *The Earth,* Cambridge Univ. Press.

Kameyama, M., Yuen, D.A. & Karato, S.-I., 1999. Thermal-mechanical effects of low-temperature plasticity (the Peierls mechanism) on the deformation of a viscoelastic shear zone, *Earth planet. Sci. Lett.,* **168,** 159–172.

Kanamori, H., 1980. The state of stress in the Earth's lithosphere, in *Physics of the Earth's Interior,* pp. 531–554, ed.,, J. Van Mieghem, Academic Press.

Karato, S., 2008. *Deformation of Earth Materials,* Cambridge Univ. Press.

Kirby, S.H., 1983. Rheology of the lithosphere, *Rev. Geophys.,* **21,** 1458–1487.

Kohlstedt, D.L., Evans, B. & Mackwell, S.J., 1995. Strength of the lithosphere—constraints imposed by laboratory experiments, *J. geophys. Res.,* **100,** 17 587–17 602.

Küster, M. & Stöckhert, B., 1999. High differential stress and sublitho-static pore fluid pressure in the ductile regime—microstructural evidence for short-term post-seismic creep in the Sesia Zone, Western Alps, *Tectonophysics,* **303,** 263–277.

Lal, D. *et al.*, 2004. Erosion history of the Tibetan Plateau since the last interglacial: constraints from the first studies of cosmogenic 10Be from Tibetan bedrock, *Earth planet. Sci. Lett.,* **217,** 33–42.

Lechmann, S.M., Schmalholz, S.M., Hetényi, G., May, D.A. & Kaus, B.J.P., 2014. Quantifying the impact of mechanical layering and underthrusting on the dynamics of the modern India-Asia collisional system with 3-D numerical models, *J. geophys. Res.,* **119,** 616–644.

Lemiale, V., Muhlhaus, H.B., Moresi, L. & Stafford, J., 2008. Shear banding analysis of plastic models formulated for incompressible viscous flows, *Phys. Earth planet. Inter.,* **171,** 177–186.

Liu, M. & Yang, Y., 2003. Extensional collapse of the Tibetan Plateau: Results of three-dimensional finite element modeling, *J. geophys. Res.,* **108**.

Lu, H., Tian, X., Yun, K. & Li, H., 2018. Convective removal of the Tibetan Plateau mantle lithosphere by ∼26 Ma, *Tectonophysics,* **731–732,** 17–34.

Madariaga, R., 1977. Implications of stress-drop models of earthquakes for the inversion of stress drop from seismic observations, *Stress in the Earth,* pp. 301–316, ed., ,Wyss, M., Birkhäuser.

McGarr, A. & Gay, N., 1978. State of stress in the earth's crust, *Annu. Rev. Earth Planet. Sci.,* **6,** 405–436.

Medvedev, S., 2016. Understanding lithospheric stresses: systematic analysis of controlling mechanisms with applications to the African Plate, *Geophys. J. Int.,* **207,** 393–413.

Medvedev, S.E. & Podladchikov, Y.Y., 1999a. New extended thin-sheet approximation for geodynamic applications - I. Model formulation, *Geophys. J. Int.,* **136,** 567–585.

Medvedev, S.E. & Podladchikov, Y.Y., 1999b. New extended thin-sheet approximation for geodynamic applications - II. Two-dimensional examples, *Geophys. J. Int.,* **136,** 586–608.

Molnar, P., Boos, W.R. & Battisti, D.S., 2010. Orographic controls on climate and paleoclimate of Asia: thermal and mechanical roles for the Tibetan Plateau, *Annu. Rev. Earth Planet. Sci.,* **38,** 77–102.

Molnar, P., England, P. & Martinod, J., 1993. Mantle dynamics, uplift of the Tibetan plateau, and the Indian monsoon, *Rev. Geophys.,* **31,** 357–396.

Molnar, P. & Lyon-Caen, H., 1988. Some simple physical aspects of the support, structure and evolution of mountain belts, *Geol. Soc. Am. Spec. Pap.,* **218,** 179–207.

Moulas, E., Burg, J.-P. & Podladchikov, Y., 2014. Stress field associated with elliptical inclusions in a deforming matrix: mathematical model and implications for tectonic overpressure in the lithosphere, *Tectonophysics,* **631,** 37–49.

Moulas, E., Schmalholz, S.M., Podladchikov, Y., Tajčmanová, L., Kostopoulos, D. & Baumgartner, L. 2018. Relation between mean stress, thermodynamic and lithostatic pressure, *J. Metamorphic Geol.,* in press, doi.org/10.1111/jmg.12446.

Métivier, F., Gaudemer, Y., Tapponnier, P. & Klein, M., 1999. Mass accumulation rates in Asia during the Cenozoic, *Geophys. J. Int.,* **137,** 280–318.

Nabelek, J. *et al.*, 2009. Underplating in the Himalaya–Tibet collision zone revealed by the Hi-CLIMB experiment, *Science,* **325,** 1371–1374.

Nadeau, R.M. & Johnson, L.R., 1998. Seismological studies at Parkfield VI: Moment release rates and estimates of source parameters for small repeating earthquakes, *Bull. seism. Soc. Am.,* **88,** 790–814.

Petrini, K. & Podladchikov, Y., 2000. Lithospheric pressure-depth relationship in compressive regions of thickened crust, *J. Metamorphic Geol.,* **18,** 67–77.

Popov, A.A. & Sobolev, S.V., 2008. SLIM3D: a tool for three-dimensional thermo mechanical modeling of lithospheric deformation with elasto-visco-plastic rheology, *Phys. Earth planet. Inter.,* **171,** 55–75.

Quade, J., Breecker, D.O., Daëron, M. & Eiler, J., 2011. The paleoaltimetry of Tibet: an isotopic perspective, *Am. J. Sci.,* **311,** 77–115.

Richter, B., Stünitz, H. & Heilbronner, R., 2016. Stresses and pressures at the quartz-to-coesite phase transformation in shear deformation experiments, *J. geophys. Res.: Solid Earth,* **121,** 8015–8033.

Rowley, D.B. & Currie, B.S., 2006. Palaeo-altimetry of the late Eocene to Miocene Lunpola basin, central Tibet, *Nature,* **439,** 677–681.

Sastri, V.V., Bhandari, L.L., Raju, A.T.R. & Datta, A.K., 1971. Tectonic framework and subsurface stratigraphy of the Ganga basin, *J. Geol. Soc. India,* **12,** 222–&.

Schelling, D., 1992. The tectonostratigraphie and structure of the eastern Nepal Himalaya, *Tectonics,* **11,** 925–943.

Schmalholz, S.M. & Fletcher, R.C., 2011. The exponential flow law applied to necking and folding of a ductile layer, *Geophys. J. Int.,* **184,** 83–89.

Schmalholz, S.M., Kaus, B.J.P. & Burg, J.P., 2009. Stress-strength relationship in the lithosphere during continental collision, *Geology,* **37,** 775–778.

Schmalholz, S.M. & Maeder, X., 2012. Pinch-and-swell structure and shear zones in viscoplastic layers, *J. Struct. Geol.,* **37,** 75–88.

Schmalholz, S.M. & Mancktelow, N.S., 2016. Folding and necking across the scales: a review of theoretical and experimental results and their applications, *Solid Earth,* **7,** 1417–1465.

Schmalholz, S.M., Medvedev, S., Lechmann, S.M. & Podladchikov, Y., 2014. Relationship between tectonic overpressure, deviatoric stress, driving force, isostasy and gravitational potential energy, *Geophys. J. Int.,* **197,** 680–696.

Schmalholz, S.M. & Podladchikov, Y.Y., 2000. Finite amplitude folding: transition from exponential to layer length controlled growth, *Earth planet. Sci. Lett.,* **181,** 617–633.

Schmalholz, S.M. & Podladchikov, Y.Y., 2013. Tectonic overpressure in weak crustal-scale shear zones and implications for the exhumation of high-pressure rocks, *Geophys. Res. Lett.,* **40,** 1984–198.

Schmalholz, S.M., Podladchikov, Y.Y. & Schmid, D.W., 2001. A spectral/finite difference method for simulating large deformations of heterogeneous, viscoelastic materials, *Geophys. J. Int.,* **145,** 199–208.

Shin, Y.H. *et al.*, 2015. Moho topography, ranges and folds of Tibet by analysis of global gravity models and GOCE data, *Sci. Rep.,* **5**.

Stipp, M., Stünitz, H., Heilbronner, R. & Schmid, S.M., 2002. Dynamic recrystallization of quartz: correlation between natural and experimental conditions, *Geol. Soc. Lond. Spec. Publ.*, **200,** 171–190.

Sullivan, W. & Monz, M., 2016. Rheologic evolution of low-grade metasedimentary rocks and granite across a large strike-slip fault zone: a case study of the Kellyland fault zone, Maine, USA, *J. Struct. Geol.,* **86,** 13–31.

Tajcmanova, L., Vrijmoed, J. & Moulas, E., 2015. Grain-scale pressure variations in metamorphic rocks: implications for the interpretation of petrographic observations, *Lithos,* **216–217,** 338–351.

Thielmann, M. & Kaus, B.J.P., 2012. Shear heating induced lithospheric-scale localization: does it result in subduction?, *Earth planet. Sci. Lett.,* **359,** 1–13.

Tilmann, F., Ni, J. & Team, I.I.S., 2003. Seismic imaging of the downwelling Indian lithosphere beneath central Tibet, *Science,* **300,** 1424–1427.

Townend, J. & Zoback, M.D., 2000. How faulting keeps the crust strong, *Geology,* **28,** 399–402.

Trepmann, C.A. & Stöckhert, B., 2009. Microfabric of folded quartz veins in metagreywackes: dislocation creep and subgrain rotation at high stress, *J. Metamorphic Geol.,* **27,** 555–570.

Tunini, L., Jiménez-Munt, I., Fernandez, M., Vergés, J., Villaseñor, A., Melchiorre, M. & Afonso, J.C., 2016. Geophysical–petrological model of the crust and upper mantle in the India–Eurasia collision zone, *Tectonics,* **35,** 1642–1669.

Turcotte, D. & Schubert, G., 2014. *Geodynamics,* Cambridge Univ. Press.

Twiss, R.J., 1977. Theory and applicability of a recrystallized grain-size paleopiezometer, *Pure appl. Geophys.,* **115,** 227–244.

Vozar, J., Jones, A.G., Fullea, J., Agius, M.R., Lebedev, S., Le Pape, F. & Wei, W., 2014. Integrated geophysical–petrological modeling of lithosphere–asthenosphere boundary in central Tibet using electromagnetic and seismic data, *Geochem. Geophys. Geosyst.,* **15,** 3965–3988.

Wittlinger, G., Farra, V., Hetényi, G., Vergne, J. & Nabelek, J., 2009. Seismic velocities in Southern Tibet lower crust: a receiver function approach for eclogite detection, *Geophys. J. Int.,* **177,** 1037–1049.

Xu, Q., Ding, L., Zhang, L., Cai, F., Lai, Q., Yang, D. & Liu-Zeng, J., 2013. Paleogene high elevations in the Qiangtang Terrane, central Tibetan Plateau, *Earth planet. Sci. Lett.,* **362,** 31–42.

Zhao, J. *et al.*, 2010. The boundary between the Indian and Asian tectonic plates below Tibet, *Proc. Natl. Acad. Sci. USA,* **107,** 11229–11233.

APPENDIX A

The kinematic model of the traditional thin-sheet approximation (England & McKenzie 1982) assumes that the horizontal velocity is constant with depth, so that the depth integral of σ_{xx}^{ts} corresponds to the driving horizontal force per unit length, $\overline{\sigma_{xx}^{ts}} = F_x$. To derive eq. (23) we assume that $\prod(\sigma_{xx}^{ts}) = 0$, which is true only for certain properties of the reference level for bending, $w(x)$, namely,

$$\overline{\sigma_{xx}^{ts}(z-w)} = 0 \quad \Rightarrow \quad \overline{\sigma_{xx}^{ts}z} - F_x w = 0$$
$$\Rightarrow \quad w = \overline{\sigma_{xx}^{ts}z}/F_x. \tag{A1}$$

For a viscoplastic lithosphere, the values of σ_{xx}^{ts} are controlled by a depth-dependent effective viscosity, η_{eff}, and for a depth-uniform strain rate the expression for $w(x)$ in eq. (A1) becomes $w = \overline{\eta_{eff}z}/\overline{\eta_{eff}}$. For the lithospheric model considered here, the appropriate value of $w(x)$ can be calculated only numerically and it varies also in space and with time. Generally, $w(x)$ should be located close to the level of the maximum strength in the lithosphere. If the system would be characterized by more than one distinct 'strength maxima', the system is unlikely to be treatable with the thin-sheet approximation of bending stresses with any accuracy.

The moment of the lithospheric pressure, $\prod(P_L)$, can be evaluated using formulae for moment evaluations in a two-layer system with a laterally variable crustal thickness, $h_c(x)$, and lithospheric mantle thickness, $h_m(x)$, (Medvedev & Podladchikov 1999b):

$$\Pi(P_L) = \int_{Sb}^{St(x)} (z-w) \int_z^{St(x)} \rho(x,z')\, g\, dz'\, dz =$$
$$= \left(\frac{h_c(x)^3}{3} + \frac{h_m(x)^2 h_c(x)}{2}\right) \rho_c g + \frac{h_m(x)^3}{3}\rho_m g$$
$$- [St(x) - w(x)]\, GPE. \tag{A2}$$

Assuming local isostasy, the geometry of the lithosphere can be expressed as a single function of the laterally variable elevation, $h_{ex} = St(x) - St(\text{lowland})$:

$$h_c(x) = h_c + h_{ex}\frac{\rho_m}{\rho_m - \rho_c}$$
$$h_m(x) = h_m - h_{ex}\frac{\rho_c}{\rho_m - \rho_c} \tag{A3}$$
$$St(x) - w(x) = h_{ex} + W = h_{ex} + w_1 h_{ex} + w_0,$$

where h_c and h_m are initial thicknesses of the crust and lithospheric mantle in the lowland, both independent from x, and $W = w_1 h_{ex} + w_0$ is the positive distance from the topography of the lowland to the reference line $w(x)$. We express all the parts of $\prod(P_L)$ from eq. (A2) as a polynomial of h_{ex} using the following relations:

$$\left(\frac{h_c(x)^3}{3} + \frac{h_m(x)^2 h_c(x)}{2}\right)\rho_c g + \frac{h_m(x)^3}{3}\rho_m g = h_{ex}^3 A_1 g + h_{ex}^2 B_1 g$$
$$+ h_{ex} C_1 + D_1$$
$$h_{ex} GPE = h_{ex}^3 A_2 g + h_{ex}^2 B_2 g + h_{ex} C_2 \tag{A4}$$
$$W \cdot GPE = h_{ex}^3 w_1 A_2 g + h_{ex}^2 g [w_1 B_2 + w_0 A_2] + W \cdot C_2$$
$$[St(x) - w(x)]\, GPE = h_{ex}^3 (1 + w_1) A_2 g$$
$$+ h_{ex}^2 [(1 + w_1) B_2 + w_0 A_2] g + ...$$

In the polynomial expression we only need coefficients for the second and third power of h_{ex} since we use the polynomial only in

eq. (23) with the second derivative of $\prod(P_L)$. The required coefficients are as follows:

$$A_1 = \frac{\rho_c \rho_m}{(\rho_m - \rho_c)^3}\left(\frac{\rho_m^2}{3} + \frac{\rho_c \rho_m}{2} - \frac{\rho_c^2}{3}\right)$$
$$B_1 = \frac{h_c \rho_c}{(\rho_m - \rho_c)^2}\left(\rho_m^2 + \frac{\rho_c^2}{2}\right) \tag{A5}$$
$$A_2 = \frac{\rho_c \rho_m}{2(\rho_m - \rho_c)}$$
$$B_2 = h_c \rho_c.$$

The coefficients A and B used in eq. (24) are then

$$A = [A_1 - (1 + w_1) A_2]\, g$$
$$B = [B_1 - (1 + w_1) B_2 - w_0 A_2]\, g. \tag{A6}$$

Several properties of the resulting bending moment and characteristic bending stress are important to mention: (1) Neither part of the density moment $\prod(P_L)$ that contributes to bending stress estimates (eqs A1–A3) nor GPE evaluation (eq. 16) depends on h_m. As discussed in Section 2, the principal contribution of integrated stresses and moments results from the stress bearing areas, characterized by ERT, which is not related to the chosen depth of compensation. That makes the total depth of the model lithosphere an inadequate measure of the characteristic length scale in the thin-sheet model. That is in contrast with the usage of the depth of compensation as the characteristic length-scale measure in the thin-sheet approximation introduced by England & McKenzie (1982). (2) ERT and $w(x)$ are two approximate parameters that control the characteristic bending stress. Whereas the dependence on ERT is clear from eq. (27), the dependence on the reference surface $w(x)$ is not obvious. To illustrate the dependence on $w(x)$, we calculate the moment for another reference surface $w'(x)$ and consider the difference:

$$\prod(\sigma_{xx}^d) - \prod{}'(\sigma_{xx}^d) = \overline{\sigma_{xx}^d(z-w)} - \overline{\sigma_{xx}^d(z-w')}$$
$$= F_x(w' - w). \tag{A7}$$

Using eqs (17) and (28) and assuming that ERT is the same for in-plane and for bending stresses, eq. (A7) can be rearranged to yield:

$$\tau_{xx}^b\big|_{w'} = \tau_{xx}^b\big|_{w'} + \frac{6(w' - w)}{ERT}\tau_{xx}^*. \tag{A8}$$

The resulting stress depends, hence, linearly on the choice of $w(x)$. The low angle of the isolines for stress in Fig. 5(b) demonstrates the minor dependence of bending stress on the choice of $w(x)$ because magnitudes of bending stresses are substantially larger than magnitudes of characteristic membrane stresses, that is, $\tau_{xx}^b > \tau_{xx}^*$. This inequality is justified if we compare maximum values of τ_{xx}^b in Fig. 5 with estimates for τ_{xx}^* from eq. (18). This inequality in combination with eq. (A8) also validates the use of an arbitrary chosen $w(x)$ instead of the use of the exact value of $w(x)$ given in eq. (A1).

APPENDIX B

The applied numerical algorithm solves the partial differential equations of continuum mechanics for 2-D slow deformations (no inertia) coupled with heat transfer under gravity. The force balance equations are:

$$\frac{\partial \sigma_{ij}}{\partial x_j} = -\rho b_i \tag{B1}$$

where i and j are indexes of either 1 or 2 and represent the horizontal x-direction ($i, j = 1$) and vertical y-direction ($i, j = 2$), $b_1 = 0$ and $b_2 = g$. σ_{ij} are the total Maxwell-viscoelastic stress tensor components which are expressed using a backward-Euler rule (e.g. Schmalholz *et al.* 2001) by

$$\sigma_{ij} = -P + 2\left(\frac{1}{\eta} + \frac{1}{G\Delta t}\right)^{-1}\dot{\varepsilon}_{ij}$$
$$+ \left(1 + \frac{G\Delta t}{\eta}\right)^{-1}\sigma_{ij}^o + J_{ij}, \tag{B2}$$

where P corresponds to the pressure, $\dot{\varepsilon}_{ij}$ are the components of the deviatoric strain rate tensor, G is the shear modulus, η is the effective viscosity, Δt is the numerical time step, σ_{ij}^o are the stress tensor components from the previous time step and J_{ij} includes all the corresponding terms resulting from the Jaumann rate of the stress tensor (e.g. Beuchert & Podladchikov 2010).

The rheological model is based on the additive decomposition of the deviatoric strain rate tensor $\dot{\varepsilon}_{ij}$:

$$\dot{\varepsilon}_{ij} = \dot{\varepsilon}_{ij}^{el} + \dot{\varepsilon}_{ij}^{pl} + \dot{\varepsilon}_{ij}^{dis} + \dot{\varepsilon}_{ij}^{dif} + \dot{\varepsilon}_{ij}^{pe}, \tag{B3}$$

where $\dot{\varepsilon}_{ij}^{el}$, $\dot{\varepsilon}_{ij}^{pl}$, $\dot{\varepsilon}_{ij}^{dis}$, $\dot{\varepsilon}_{ij}^{dif}$ and $\dot{\varepsilon}_{ij}^{pe}$, respectively, correspond to the strain rate contributions arising from elasticity, plasticity and viscous creep (dislocation, diffusion and Peierls). This strain rate equation is nonlinear and solved locally on cell centroids and vertices in order to define the current effective viscosity and stress (e.g. Popov & Sobolev 2008). The viscosity for dislocation creep is a function of the dislocation creep strain rate invariant, $\dot{\varepsilon}_{II}^{dis} = \tau_{II}/2\eta^{dis}$,

$$\eta^{dis} = \frac{2^{\frac{1-n}{n}}}{3^{\frac{1+n}{2n}}} A\left(\dot{\varepsilon}_{II}^{dis}\right)^{\frac{1}{n}-1}\exp\left(\frac{Q + PV}{nRT}\right) \tag{B4}$$

where the ratio involving the stress exponents to the left of A results from the conversion of the experimentally derived 1-D flow law to a general flow law for tensor components based on invariants (e.g. Gerya 2010; Schmalholz & Fletcher 2011). Applied parameters are displayed in Table 1. Diffusion creep is taken into account in the lithospheric and asthenospheric mantle and its viscosity is expressed as

$$\eta^{dif} = A\, d^m \exp\left(\frac{Q + PV}{RT}\right), \tag{B5}$$

where d is grain size and m is grain size exponent (Table 1). Peierls creep (i.e. low-temperature plasticity) is applied only in the mantle lithosphere with parameters from Goetze & Evans (1979) using the formulation of Kameyama *et al.* (1999). The viscosity corresponding to Peierls creep takes the following form:

$$\eta^{pe} = \frac{2^{\frac{1-s}{s}}}{3^{\frac{1+s}{2s}}} A\left(\dot{\varepsilon}_{II}^{pe}\right)^{\frac{1}{s}-1}, \tag{B6}$$

where s is an effective stress exponent that depends on the temperature:

$$s = 2\gamma\frac{Q}{RT}(1 - \gamma). \tag{B7}$$

The A for this formulation is

$$A = \left[A_p \exp\left(-\frac{Q(1-\gamma)^2}{RT}\right)\right]^{-\frac{1}{s}}\gamma\sigma_p \tag{B8}$$

where γ is a fitting parameter from the Peierls flow law (Table 1).

The stress of all material phases is limited by a yield stress, τ_y, defined by the Drucker–Prager criterion

$$\tau_y = b\cos(\theta) + P\sin(\theta), \tag{B9}$$

where b is the cohesion and θ is the angle of internal friction. In case of yielding, the effective viscosity is iteratively reduced until the corresponding stress invariant equals the yield stress (e.g. Lemiale *et al.* 2008; Schmalholz & Maeder 2012). Therefore, the effective viscosity for plasticity is computed only for $\tau_{II} - \tau_y \geq 0$ and takes the form of

$$\eta^{pl} = \frac{\tau_y}{2\dot{\varepsilon}_{II}^{pl}}\,\text{if}\,\tau_{II} - \tau_y \geq 0, \tag{B10}$$

where $\dot{\varepsilon}_{II}^{pl}$ is the second invariant of the plastic strain rate tensor having components $\dot{\varepsilon}_{ij}^{pl}$ (eq. B3).

At the end of the local iteration cycle, the effective viscosity is equal to the harmonic mean of the viscosities of each dissipative deformation mechanism:

$$\eta = \left(\frac{1}{\eta^{dis}\left(\dot{\varepsilon}_{II}^{dis}\right)} + \frac{1}{\eta^{dif}\left(\dot{\varepsilon}_{II}^{dif}\right)} + \frac{1}{\eta^{pe}\left(\dot{\varepsilon}_{II}^{pe}\right)} + \frac{1}{\eta^{pl}\left(\dot{\varepsilon}_{II}^{pl}\right)}\right)^{-1}. \tag{B11}$$

Eq. (B11) indicates that each viscosity is calculated with the respective second strain rate invariant, which is calculated from the strain rate tensor components of the corresponding deformation mechanism (eq. B3).

The applied 2-D equation for heat transfer is

$$\rho c\frac{DT}{Dt} = \frac{\partial}{\partial x_i}\left(k\frac{\partial T}{\partial x_i}\right) + H_D + H_R \tag{B12}$$

with D/Dt representing the total time derivative, H_R being radiogenic heat production and $H_D = (\tau_{11}^2 + \tau_{22}^2 + 2\tau_{12}^2)/2\eta$ being the heating due to viscous and plastic dissipative work. We assume here that all dissipative work is converted into heat (i.e. the so-called Taylor–Quinney coefficient is 1) since we do not model grain size reduction which consumes typically only a minor fraction of the dissipative work.